

1 **A synthetic peptide that prevents cAMP regulation in mammalian Hyperpolarization-**
2 **activated Cyclic Nucleotide-regulated (HCN) channels**

3 Andrea Saponaro¹, Francesca Cantini², Alessandro Porro¹, Annalisa Bucchi¹, Dario
4 DiFrancesco¹, Vincenzo Maione², Chiara Donadoni¹, Bianca Introini¹, Pietro Mesirca^{3,8},
5 Matteo E. Mangoni^{3,8}, Gerhard Thiel⁴, Lucia Banci^{2,5}, Bina Santoro⁶, Anna Moroni^{1,7}

6 ¹Department of Biosciences University of Milan, Italy;

7 ²Centro Risonanze Magnetiche (CERM) and Department of Chemistry, University of
8 Florence, Italy;

9 ³Institut de Génomique Fonctionnelle, Université de Montpellier, CNRS, INSERM, F-
10 34094, Montpellier, France.

11 ⁴Department of Biology, TU-Darmstadt, Darmstadt, Germany;

12 ⁵Institute of Neurosciences, Consiglio Nazionale delle Ricerche, Florence, Italy

13 ⁶Department of Neuroscience, Columbia University, New York, USA;

14 ⁷Institute of Biophysics, Consiglio Nazionale delle Ricerche, Milan, Italy.

15 ⁸Laboratory of Excellence (LabEx) Ion Channels Science and Therapeutics (ICST).

16 * Corresponding author: Anna Moroni, Department of Biosciences, Via Celoria 26, 20133
17 Milano, Italy, tel. + 39 12 50314826, email: anna.moroni@unimi.it

18

19

20

21 **Abstract**

22 Binding of TRIP8b to the cyclic nucleotide binding domain (CNBD) of mammalian HCN
23 channels prevents their regulation by cAMP. Since TRIP8b is expressed exclusively in the
24 brain, we envisage that it can be used for orthogonal control of HCN channels beyond the
25 central nervous system. To this end, we have identified by rational design a 40-aa long
26 peptide (TRIP8b_{nano}) that recapitulates affinity and gating effects of TRIP8b in HCN
27 isoforms (human hHCN1, mHCN2, rbHCN4) and in the cardiac current I_f in rabbit and
28 mouse sinoatrial node cardiomyocytes. Guided by a NMR-derived structural model that
29 identifies the key molecular interactions between TRIP8b_{nano} and HCN CNBD, we further
30 designed a cell-penetrating peptide (TAT-TRIP8b_{nano}) which successfully prevented b-
31 adrenergic activation of mouse I_f leaving the stimulation of the L-type calcium current (I_{CaL})
32 unaffected. TRIP8b_{nano} represents a novel approach to selectively control HCN activation,
33 which yields the promise of a more targeted pharmacology compared to pore blockers.

34

35

36

37

38

39

40 Keywords: HCN channels/TRIP8b/cAMP/allosteric inhibition/direct competition

41

42

43 **Introduction**

44 Hyperpolarization-activated cyclic nucleotide-regulated (HCN1-4) channels are the
45 molecular correlate of the I_f/I_h current, which plays a key role in controlling several higher
46 order physiological functions, including dendritic integration and intrinsic rhythmicity both in
47 cardiac and neuronal cells (Robinson & Siegelbaum, 2003). Unique among the voltage-
48 gated ion channel superfamily, HCN channels are modulated by the direct binding of
49 cAMP to their cyclic nucleotide binding domain (CNBD). Binding of the cyclic nucleotide
50 increases the channel open probability upon hyperpolarization via conformational changes
51 in the CNBD that are propagated to the pore through the C-linker domain (DiFrancesco &
52 Tortora, 1991; Wainger, DeGennaro, Santoro, Siegelbaum, & Tibbs, 2001; Weissgraeber,
53 Saponaro, Thiel, & Hamacher, 2017; Zagotta et al., 2003).

54 In addition to cAMP, HCN channels are regulated by TRIP8b, a brain-specific auxiliary (β)
55 subunit, which modulates two independent features of the channel namely trafficking and
56 gating (Bina Santoro et al., 2009; Zolles et al., 2009). For this dual regulation TRIP8b
57 binds HCN channels in two distinct sites: *via* the tetratricopeptide repeat (TPR) domain,
58 which interacts with the last three amino acids (SNL) of HCN channels and regulates their
59 trafficking; and *via* the TRIP8b_{core} domain, which interacts with the CNBD and antagonizes
60 the effect of cAMP on the voltage dependency of the channel (Bankston, DeBerg, Stoll, &
61 Zagotta, 2017; Deberg et al., 2015; Han et al., 2011; Hu et al., 2013).

62 Here we focus our attention on the specific action of TRIP8b in preventing cAMP
63 regulation of HCN channels. Given the brain-specific localization of TRIP8b, we posit that
64 a TRIP8b-derived peptide drug, able to reproduce the effect of the full length protein on
65 HCN channel gating, can be developed for orthogonal selective regulation of HCN in
66 cells/tissues in which TRIP8b is not expressed. cAMP dependent modulation of HCN
67 channels underlies distinct roles of cAMP in heart rate regulation (DiFrancesco, 1993) and

68 development of peripheral neuropathic pain (Emery, Young, & McNaughton, 2012;
69 Herrmann et al., 2017) which can be dissected by using a TRIP8b-based tool. In this
70 regard, peptide-based drugs (2-50 aa long) are emerging as a fascinating application area
71 as they open new therapeutic possibilities with an advantage over small molecules in
72 terms of specificity and affinity for the target (Fosgerau & Hoffmann, 2015; Henninot,
73 Collins, & Nuss, 2017). To this end, we searched for the minimal peptide that binds to the
74 CNBD and recapitulates the gating effect of full length TRIP8b in three HCN isoforms
75 (HCN1, HCN2 and HCN4) and in the native I_f current. In previous studies we identified the
76 core portion of TRIP8b (TRIP8b_{core}, 80 aa long) that interacts with HCN CNBD and
77 prevents cAMP modulation in full length channels (Hu et al., 2013; B. Santoro et al., 2011).
78 A recent paper (Lyman et al., 2017) reported an even shorter binding sequence of TRIP8b
79 (37 aa). However, this peptide, which was identified by progressive truncation of
80 TRIP8b_{core}, failed to reproduce the binding affinity of the starting construct. Moreover,
81 evidence for activity of this peptide on HCN currents is lacking. In the present work, we
82 adopted a structure-driven rational desing approach to engineer a 40 aa long peptide,
83 TRIP8b_{nano}, that efficiently prevents cAMP regulation of HCN channels. The rational
84 design of this peptide, based on secondary structure predictions and on NMR data of
85 TRIP8b_{core}, was supported by an NMR-based 3D model structure of the complex formed
86 by the TRIP8b_{nano} peptide and the CNBD of human HCN2 channel isoform. This structural
87 information identifies crucial interactions between the two partners and explains both direct
88 (Bankston, DeBerg, Stoll, & Zagotta, 2017; Deberg et al., 2015; Han et al., 2011) and
89 indirect (allosteric) (Bankston et al., 2017; Han et al., 2011; Hu et al., 2013; Saponaro et
90 al., 2014) modes of competition between TRIP8b and cAMP for binding to the CNBD. The
91 evidence that TRIP8b_{nano} establishes all relevant interactions with the CNBD is reflected
92 by the finding that, contrary to shorter core sequences (Lyman et al., 2017), it binds to the
93 isolated CNBD with identical affinity to TRIPb_{core} and acts with even higher efficacy than

94 TRIP8b_{core} in preventing cAMP modulation of full length HCN channels (Hu et al., 2013). In
95 pacemaker myocytes of the sino-atrial node (SAN), TRIP8b_{nano} equally prevents cAMP
96 stimulation of native f-channels leading to a 30% reduction in spontaneous firing rate.

97 To develop TRIP8b_{nano} as a membrane permeable drug, we linked it with the positively
98 charged TAT sequence (Herce, Garcia, & Cardoso, 2014). TAT-TRIP8b_{nano} was tested in
99 SAN pacemaker myocytes where its addition to the extracellular buffer prevented
100 adrenergic stimulation of the I_f current leaving the activation of the L-type calcium current
101 (I_{CaL}) unaffected. Our study opens the possibility of selective *in vivo* control of the cAMP-
102 dependent facilitation of HCN channel opening, by local supply of TAT-TRIP8b_{nano} peptide.

103

104 **Results**

105 We have previously shown that TRIP8b_{core} (residues 223 - 303 of mouse TRIP8b splice
106 variant 1a4, hereafter TRIP8b) interacts with two elements of the isolated CNBD protein
107 fragment from HCN channels (residues 521 - 672 of human HCN2, hereafter CNBD): the
108 C-helix and the N-bundle loop, a sequence connecting helix E' of the C-linker with helix A
109 of the CNBD (Saponaro et al., 2014). Biochemical assays confirmed that each of these
110 two elements, i.e. the N-bundle loop and C-helix, is necessary but not sufficient for binding
111 (Saponaro et al., 2014).

112 To understand the interaction in atomic details, we used solution NMR spectroscopy to
113 characterize the structural properties of the CNBD - TRIP8b_{core} complex. However, the
114 NMR spectra of TRIP8b_{core} showed very few signals. In order to improve the quality of the
115 NMR spectra, we reduced the length of the TRIP8b fragment by progressively removing
116 residues at the N- and C-termini with no predicted secondary structure. The truncated
117 peptides were then tested for CNBD binding activity by isothermal titration calorimetry

118 (ITC). We thus identified a 40-aa peptide (TRIP8b_{nano}, comprising residues 235 – 275 of
119 TRIP8b, *Figure 1A*) with a binding K_D of $1.5 \pm 0.1 \mu\text{M}$, a value similar to the K_D of 1.2 ± 0.1
120 μM obtained with TRIP8b_{core} (*Figure 1B*). TRIP8b_{nano} was therefore employed for all
121 subsequent NMR experiments, resulting in a remarkable improvement in the spectral
122 quality and sample stability.

123 **Structural characterization of TRIP8b_{nano} bound to CNBD**

124 The comparison of the ^1H - ^{15}N HSQC spectra of TRIP8b_{nano} with and without CNBD bound
125 shows that the peptide folds upon interaction with the CNBD. Thus, the ^1H - ^{15}N HSQC
126 spectrum of TRIP8b_{nano} without CNBD shows a limited ^1H resonance dispersion,
127 characteristic of unstructured proteins (Dyson & Wright, 2004), while a larger number of
128 well-dispersed amide signals appear in the spectrum of the CNBD-bound form (*Figure*
129 *1C*). Importantly, we were now able to assign the backbone chemical shift resonances of
130 TRIP8b_{nano} bound to the CNBD. The ϕ and ψ dihedral angles obtained from the NMR
131 assignment indicate that the peptide displays two α -helices (stretch L₂₃₈-E₂₅₀ named helix
132 N and stretch T₂₅₃-R₂₆₉ named helix C) when bound to CNBD. The helices are separated
133 by two amino acids; three and six residues at the N- and C- termini, respectively, are
134 unstructured (*Figure 1D*).

135 **Structural characterization of CNBD bound to TRIP8b_{nano}**

136 NMR-analysis of the CNBD fragment bound to TRIP8b_{nano} revealed that the interaction
137 with the peptide does not affect the overall fold of the protein. Thus, the CNBD adopts the
138 typical fold of the cAMP-free state, in line with previous evidence that this is the form
139 bound by TRIP8b (Deberg et al., 2015; Saponaro et al., 2014). More specifically, the
140 secondary structure elements of the cAMP-free CNBD are all conserved in the
141 TRIP8b_{nano}-bound CNBD (*Figure 2*). This finding generally agrees with a previous double
142 electron-electron resonance (DEER) analysis of the CNBD - TRIP8b interaction, which

143 showed that TRIP8b binds to a conformation largely similar to the cAMP-free state
144 (Deberg et al., 2015). Despite the overall agreement with the DEER study, the NMR data
145 also reveal a new and unexpected feature of TRIP8b binding to the CNBD. Indeed, our
146 results show that TRIP8b_{nano} binding to the CNBD induces a well-defined secondary
147 structure of the distal region of the C-helix (*Figure 2*). This means that the distal region of
148 the C-helix (residues 657-662), which is unstructured in the free form of the CNBD (Lee &
149 MacKinnon, 2017; Saponaro et al., 2014), extends into a helical structure upon ligand
150 binding irrespectively of whether the ligand is cAMP (Lee & MacKinnon, 2017; Puljung &
151 Zagotta, 2013; Saponaro et al., 2014) or TRIP8b (*Figure 2*). In contrast, and very
152 differently from cAMP, which directly contacts the P-helix in the Phosphate Binding
153 cassette (PBC) and causes its folding (Lee & MacKinnon, 2017; Saponaro et al., 2014),
154 the NMR data show that TRIP8b_{nano} binding to the CNBD does not induce P-helix
155 formation (*Figure 2*).

156 **Modelling the CNBD - TRIP8b_{nano} complex**

157 Despite the significant improvement in sample stability and NMR spectra quality achieved
158 upon TRIP8b_{nano} binding, we were still unable to assign the side chains of both proteins in
159 the complex and thus could not solve the solution structure of the complex by the
160 canonical NMR procedure. We therefore built a model (*Figure 3*) of the CNBD - TRIP8b_{nano}
161 complex by docking the two NMR-derived structures described above using the Haddock
162 program (a detailed description of how the respective structures were generated is
163 provided in Materials and Methods and *Figure 3-source data 1*).

164 In order to define the active residues (ambiguous interaction restraints) on the CNBD we
165 used the chemical shift perturbation values as described in *Figure 3-figure supplement 1*.
166 For TRIP8b_{nano}, we defined as active a stretch of residues, E₂₃₉-E₂₄₃, previously identified
167 as critical for the interaction (B. Santoro et al., 2011; Bina Santoro et al., 2009). Output

168 clusters of this first molecular docking calculation (settings can be found in Material and
169 Methods) were further screened for TRIP8b_{nano} orientations in agreement with a previous
170 DEER analysis, which placed TRIP8b residue A₂₄₈ closer to the proximal portion and
171 TRIP8b residue A₂₆₁ closer to the distal portion of the CNBD C-helix (Deberg et al., 2015).
172 Remarkably, in all clusters selected in this way, residues E₂₆₄ or E₂₆₅ in TRIP8b were
173 found to interact with residues K₆₆₅ or K₆₆₆ of the CNBD (*Figure 3-figure supplement 2*).
174 This finding was notable, because we previously identified K₆₆₅/K₆₆₆ as being critical for
175 TRIP8b interaction in a biochemical binding assay (Saponaro et al., 2014). We thus
176 proceeded to individually mutate each of these four positions, and test their effect on
177 binding affinity through ITC. As expected, reverse charge mutations K₆₆₅E or K₆₆₆E
178 (CNBD) as well as E₂₆₄K or E₂₆₅K (TRIP8b_{nano}) each strongly reduced the
179 CNBD/TRIP8b_{nano} binding affinity (*Figure 3-figure supplement 3*).

180 Based on these observations, we performed a second molecular docking calculation,
181 including E₂₆₄ and E₂₆₅ as additional active residues for TRIP8b_{nano}. This procedure
182 resulted in the model shown in *Figure 3*, which represents the top-ranking cluster for
183 energetic and scoring function (*Figure 3-source data 2*) and was fully validated by
184 mutagenesis analysis as described below. Scrutiny of the model shows that TRIP8b_{nano}
185 binds to both the C-helix and the N-bundle loop (*Figure 3A*). Binding to the C-helix is
186 mainly guided by electrostatic interactions between the negative charges on TRIP8b_{nano},
187 and the positive charges on the CNBD (*Figure 3A*). As shown in *Figure 3B*, the model
188 highlights a double saline bridge (K₆₆₅ and K₆₆₆ of CNBD with E₂₆₅ and E₂₆₄ of TRIP8b_{nano})
189 in line with the ITC results described above (*Figure 3-figure supplement 3*). Of note, the
190 contribution of residue R₆₆₂ to the binding is also consistent with previous experiments
191 showing residual TRIP8b interaction in a CNBD deletion mutant ending at position 663
192 (Saponaro et al., 2014). Our modelling data suggest that, upon folding of the distal portion

193 of the C-helix, the side chains of residues R₆₆₂ and K₆₆₅ face to the inside when contacting
194 cAMP, but face to the outside when binding TRIP8b (*Figure 3-figure supplement 4*). This
195 indicates that cAMP and TRIP8b directly compete for the binding to the distal region of C-
196 helix.

197 In addition to clarifying the role of residues in the distal portion of the CNBD C-helix, the
198 model also highlights a second important cluster of electrostatic interactions with R₆₅₀ in
199 the proximal portion of the CNBD C-helix contacting E₂₄₀ and E₂₄₁ in helix N of TRIP8b_{nano}
200 (*Figure 3C*). To confirm the contribution of these residues, we reversed charges and tested
201 each residue mutation for binding in ITC. The results in *Figure 3-figure supplement 3* show
202 that R₆₅₀E caused a more than six-fold reduction in binding affinity for TRIP8b_{nano}, with
203 smaller but significant effects seen also for E₂₄₀R and E₂₄₁R.

204 A third important contact highlighted by the model is the interaction between N₅₄₇ in the N-
205 bundle loop of the CNBD and D₂₅₂ in the link between helix N and helix C of TRIP8b_{nano}
206 (*Figure 3D*). We tested this potential interaction by disrupting the expected hydrogen bond
207 between N₅₄₇ and the carboxyl group of the negative residue (D₂₅₂) in TRIP8b_{nano}. The
208 asparagine in CNBD was mutated into aspartate (N₅₄₇D) to generate an electrostatic
209 repulsion for D₂₅₂, and the carboxyl group in D₂₅₂ of TRIP8b_{nano} was removed by mutation
210 into asparagine (D₂₅₂N). As predicted, N₅₄₇D greatly reduced binding to TRIP8b in ITC
211 assays (*Figure 3-figure supplement 3*), with a smaller but significant effect observed also
212 for D₂₅₂N (*Figure 3-figure supplement 3*). These results confirm and extend our previous
213 finding that the N-bundle loop contributes in a substantial manner to the binding of TRIP8b
214 (Saponaro et al., 2014). In search for the allosteric effect of TRIP8b on cAMP binding,
215 already postulated on the basis of electrophysiological and structural data (Hu et al., 2013;
216 Saponaro et al., 2014), we have further tested by ITC the affinity of N₅₄₇D CNBD mutant
217 for cAMP. Somewhat surprisingly, the affinity of the mutant is much lower than that of the

218 wt ($N_{547}D$ $K_D = 5.5 \pm 0.4 \mu M$ ($n=3$) vs. wt $K_D = 1.4 \pm 0.1 \mu M$ ($n=3$)). Moreover, we
219 measured a reduced sensitivity to cAMP also in patch clamp experiments where addition
220 of $5 \mu M$ cAMP caused a right shift in the $V_{1/2}$ of the mutant HCN2 channel of only 5 mV
221 while the wt channel shifted by 12 mV (*Figure 3-figure supplement 5*). To exclude that the
222 $N_{547}D$ mutation affects the overall structure of the CNBD, we performed the NMR (1H - ^{15}N
223 HSQC spectrum) analysis of the $N_{547}D$ CNBD mutant. Our data show that the protein is
224 appropriately folded (*Figure 3-figure supplement 6*). In conclusion, since the N-bundle loop
225 does not directly contact any of the residues of the cAMP binding pocket, these findings
226 underscore a previously unaddressed role of the N-bundle loop in allosterically modulating
227 cAMP binding to the CNBD (see Discussion).

228

229 **TRIP8b_{nano} as a tool for the direct regulation of native HCN currents**

230 Next, we asked whether the relatively short TRIP8b_{nano} could be used to block cAMP-
231 dependent modulation of HCN channels by delivering the peptide to full length channels.
232 To this end, we dialyzed TRIP8b_{nano} into the cytosol of HEK 293T cells transfected either
233 with HCN1, HCN2, or HCN4 channels. The peptide was added ($10 \mu M$) in the recording
234 pipette together with a non-saturating concentration of cAMP ($5 \mu M$ for HCN2, $1 \mu M$ for
235 HCN4) expected to induce a ~ 10 mV rightward shift in the half-activation potential ($V_{1/2}$) of
236 the channels (*Figure 4*). No cAMP was added in the case of HCN1, because, in HEK 293T
237 cells, this isoform is already fully shifted to the right by the endogenous cAMP and does
238 not respond further (*Figure 4-figure supplement 1*). Still, it is possible to induce a ~ 10 mV
239 left shift in HCN1 $V_{1/2}$ by introducing the mutation R549E that prevents cAMP binding to
240 the CNBD (*Figure 4-figure supplement 1*).

241 *Figure 4A-C* show representative currents recorded at four given voltages, in control
242 solution, + 5 μ M cAMP and + 5 μ M cAMP + 10 μ M TRIP8b_{nano} in the patch pipette (HCN4
243 and HCN2) or + 10 μ M TRIP8b_{nano} (HCN1). Already from a visual comparison of the most
244 positive voltage at which the current appears measurable, it is evident that TRIP8b_{nano}
245 counteracts the activating effect of cAMP on the voltage-dependent gating. In the case of
246 HCN1, the effect of TRIP8b_{nano} can be observed without added cAMP for the
247 aforementioned reasons. *Figure 4D-F* show the mean channel activation curves obtained
248 from the above and other experiments. Fitting the Boltzmann equation to data (solid and
249 dashed lines of *Figure 4D-F*, see Methods for equation) yielded the half-activation potential
250 values ($V_{1/2}$) plotted in *Figure 4G*. The addition of TRIP8b_{nano} prevents the cAMP-induced
251 right shift of about 13 mV in HCN4 ($V_{1/2}$ = -102.8, -89.2, -102.1 mV, for control, + cAMP
252 and + cAMP + TRIP8b_{nano}, respectively), and of about 11 mV in HCN2 ($V_{1/2}$ = -93.7, -83.5,
253 -94.5 mV, for control, + cAMP and + cAMP + TRIP8b_{nano}, respectively). In HCN1,
254 TRIP8b_{nano} induced a left shift of about 10 mV in $V_{1/2}$ (from -72.8 to -82 mV) that is
255 comparable to that induced by the R549E mutation (from -72.7 to -80.4 mV) (*Figure 4-*
256 *figure supplement 1*).

257 *Figure 4G* also shows the result of a control experiment performed on HCN4 where 10 μ M
258 TRIP8b_{nano} was added to the extracellular medium (TRIP8b_{nano} bath) in order to test if the
259 peptide was able to pass the cell membrane (current traces and activation curves not
260 shown). The $V_{1/2}$ value, which is similar to that of cAMP alone (-91.7 vs. -89.2 mV),
261 confirmed that TRIP8b_{nano} peptide affects channel gating only if added to the intracellular
262 solution presumably because it does not diffuse through the cell membrane.

263 It is worth noting that TRIP8b_{nano} prevents other related aspects of cAMP activation in
264 HCN, such as the acceleration of activation kinetics (Wainger et al., 2001) and, for HCN2
265 only, the increase in maximal current (Craven & Zagotta, 2004; Wainger et al., 2001). For

266 example, the activation kinetics (τ_{on}) of HCN4 measured at -120 mV was: control = 2 ± 0.2
267 s, + cAMP = 1.2 ± 0.1 s, + cAMP + TRIP8b_{nano} = 2 ± 0.3 s (*Figure 4-figure supplement 2*).
268 Moreover, Figure 4B clearly shows that TRIP8b_{nano} fully prevented the increase in maximal
269 current in HCN2.

270 From these results, we reckoned the peptide may be employed as a regulatory tool for
271 native I_f/I_h currents. As proof of principle, we tested whether TRIP8b_{nano} can modulate the
272 frequency of action potential firing in SAN myocytes. In these cells I_f is key contributor of
273 the diastolic depolarization phase of the pacemaker action potential cycle. Moreover, the
274 autonomic nervous system modulates the frequency of action potential firing by changing
275 intracellular cAMP levels, which in turn acts on f-HCN channel open probability
276 (DiFrancesco, 1993). We thus recorded the native I_f current in acutely isolated rabbit SAN
277 myocytes with and without 10 μ M TRIP8b_{nano} in the pipette solution (*Figure 5A*). *Figure 5B*
278 shows that the averaged I_f activation curve measured in presence of TRIP8b_{nano} is
279 significantly shifted to hyperpolarized voltages compared to the control. This indicates that
280 the peptide is displacing the binding of endogenous cAMP to native HCN channels.
281 Moreover, when the experiment was repeated in the presence of 1 μ M cAMP, TRIP8b_{nano}
282 prevented the typical cAMP-dependent potentiation of the native I_f current (*Figure 5B*). In
283 light of these results, we tested whether TRIP8b_{nano} is also able to modulate cardiac
284 automaticity by antagonizing basal cAMP. The data in *Figure 5C* show that TRIP8b_{nano}
285 indeed significantly decreased the rate of action potential firing in single SAN cells.
286 Strikingly, the observed 30% decrease in action potential rate corresponds to the effect
287 induced by physiological concentrations of acetylcholine (DiFrancesco, Ducouret, &
288 Robinson, 1989).

289 To conclusively prove that the inhibition of the native I_f current was specifically due to
290 TRIP8b_{nano} rather than caused by the dilution of the cellular content followed by whole cell

291 configuration, we created a TAT version of TRIP8b_{nano} (hereafter TAT-TRIP8b_{nano}). Indeed,
292 the TAT sequence allows the entry of biomolecules into a cell via endocytosis and/or direct
293 translocation across the plasma membrane, thus leaving the cytosolic content unaltered
294 (Guidotti, Brambilla, & Rossi, 2017).

295 We thus tested whether both TRIP8b_{nano} and TAT-TRIP8b_{nano} were able to selectively
296 inhibit the β -adrenergic stimulation of I_f current, while leaving the potentiation of L-type
297 Ca^{2+} current ($I_{Ca,L}$) unaltered. To this end, we recorded either the native I_f or $I_{Ca,L}$ current
298 from cardiomyocytes acutely isolated from mouse sinoatrial node (SAN) in the presence
299 and in the absence of 10 μ M TRIP8b_{nano} or TAT-TRIP8b_{nano}, before and after stimulation
300 with 100 nM isoproterenol (ISO), a β -adrenergic receptor agonist (*Figure 6*). Strikingly,
301 TRIP8b_{nano} prevented the isoproterenol-induced increase of I_f current density, both when
302 the peptide was added in the recording pipette solution (*Figure 6A and 6B*), and when it
303 was used in the TAT version (*Figure 6A and 6C*). The specificity of TRIP8b_{nano} for I_f current
304 was confirmed by the absence inhibition of basal $I_{Ca,L}$ (*Figure 6D*). In addition, we failed to
305 record a significant difference in the isoproterenol-stimulated increase of the $I_{Ca,L}$ current
306 density between the control condition and 10 μ M TRIP8b_{nano} (*Figure 6E*) or TAT-
307 TRIP8b_{nano} (*Figure 6F*) conditions. To test whether the TAT-TRIP8b_{nano} effect described
308 above was exclusively due to TRIP8b_{nano} peptide, we repeated the experiments with a
309 scrambled version of the peptide (TAT- (SCRAMBLED) TRIP8b_{nano}) to exclude that the
310 effect could be due to the TAT sequence (*Figure 6-figure supplement 1*). We failed to
311 observe a significant reduction in the responsiveness of I_f to isoproterenol in the presence
312 of TAT- (SCRAMBLED) TRIP8b_{nano} confirming that prevention of cAMP induced I_f - current
313 stimulation was specific of the TRIP8b_{nano} sequence.

314

315

316 **Discussion**

317 **TRIP8b-CNBD complex**

318 In this work we have identified the minimal binding peptide that reproduces the effects of
319 TRIP8b on HCN channel gating. The peptide is 40 aa long and binds the HCN CNBD with
320 high affinity ($K_D = 1.4 \mu\text{M}$). By solving the NMR structures of TRIP8b_{nano} and HCN CNBD in
321 the bound form, we generated a structural model of their complex. The model provides
322 detailed information on this protein - protein interaction at the atomic level with implications
323 on their physiological function. The data show that the minimal binding unit of TRIP8b,
324 TRIP8b_{nano}, folds in two helices upon binding and suggest that this region is intrinsically
325 disordered when it is not bound. The model structurally validates previous indirect
326 evidences, which suggested that TRIP8b binds to two discrete elements of the CNBD: the
327 N-bundle loop and the C-helix (Saponaro et al., 2014). The complex forms by electrostatic
328 interactions, which are spread throughout the contact surface. As a consequence of the
329 interaction with TRIP8b_{nano}, the C-helix of CNBD increases in length, a behavior previously
330 observed in the case of cAMP binding (Puljung & Zagotta, 2013). This portion of C-helix
331 includes the two residues R₆₆₂ and K₆₆₅ engaged in salt bridge formation with respectively
332 E₂₅₀/D₂₅₇ and E₂₆₄ of TRIP8b_{nano}. Important to note is that the two cationic residues are
333 also involved in cAMP binding (Lolicato et al., 2011; Zagotta et al., 2003; Zhou &
334 Siegelbaum, 2007). The finding that TRIP8b and cAMP share the same binding sites on
335 the C-helix provides a solid molecular explanation for functional data, which imply a
336 competition between the two regulators (Bankston et al., 2017; Deberg et al., 2015; Han et
337 al., 2011). Another study however has indicated that a direct competition model does not
338 fully explain the mutually antagonistic effect of the two ligands (Hu et al., 2013).
339 Specifically, the fact that the inhibitory effect of TRIP8b on channel activity persists even at
340 saturating cAMP concentrations advocated an allosteric component in the regulation

341 mechanism. Our data, showing that N547D mutation in the N-bundle loop controls cAMP
342 affinity in the binding pocket support the conclusion that the N-bundle loop allosterically
343 controls cAMP binding. This is not surprising, given its crucial role of mechanically
344 transducing to the pore the cAMP binding event within the CNBD (Saponaro et al., 2014).

345 The structural model also explains why a previously identified peptide selected by Lyman
346 et al (Lyman et al., 2017) failed to reproduce the binding affinity of the TRIP8b_{core} for the
347 CNBD. This 37 aa long fragment is lacking one important contact residue, namely E₂₄₀
348 that, in our model, forms a salt bridge with R₆₅₀ of the CNBD. The loss of one crucial
349 interaction is presumably the cause for such a major decrease in affinity (about 20 times
350 lower) reported for this peptide.

351 **TRIP8b_{nano} as a tool for modulating native I_f currents**

352 In functional assays we showed that TRIP8b_{nano} binds the HCN channel CNBD with high
353 affinity and fully abolishes the cAMP effect in all tested isoforms (HCN1, 2 and 4).

354 Given the small size of the peptide (<5kDa), TRIP8b_{nano} is a good candidate for an *in vivo*
355 delivery into intact cells. As a proof of concept, we fused TRIP8b_{nano} to an internalization
356 sequence, the TAT peptide (YGRKKRRQRRRGG). This arginine-rich Cell Penetrating
357 Peptide (CPP) from HIV has been used in several studies as a vehicle for the delivery of
358 large molecules across the plasma membrane (Guidotti et al., 2017). In our case, the
359 challenge was to construct a TAT-fusion protein, which is efficiently delivered in the cell
360 without compromising TRIP8b_{nano} function. Indeed, covalent conjugation of a CPP may
361 negatively affect both the function of the cargo, and the cell-penetrating efficacy of the
362 CPP-peptide chimera (Kristensen, Birch, & Morck Nielsen, 2016). The design of the
363 construct was greatly supported by the detailed knowledge of the electrostatic interactions
364 with the target protein CNBD, provided by the NMR model structure. This structure
365 suggested that the polycationic TAT sequence would be best linked to the N-terminus of

366 TRIP8b_{nano} to avoid interference with the cationic residues of CNBD, mainly located in the
 367 distal region of C-helix, which are crucial for the binding of the peptide. From test
 368 experiments with the TAT-TRIP8b_{nano} peptide in SAN myocytes we can conclude that this
 369 strategy was successful in that: i) the peptide is efficiently delivered inside the cells; ii) it is
 370 kept in its active conformation; iii) the TAT sequence did not destroy cell membranes and
 371 did not interfere with the basic features of I_f and I_{Ca,L} currents; iv) the modification did not
 372 affect the proteolytic stability of the TRIP8b_{nano} peptide at least in the time frame of our
 373 experiments (30 min to 1 hour).

374 In conclusion, we successfully used the miniaturized TRIP8b_{nano} peptide to selectively
 375 control native I_f currents and the rate of spontaneous firing in SAN myocytes. Unlike
 376 channel blockers, which inhibit ionic currents, the peptide only interferes with the cAMP-
 377 based regulation of HCN channels, while leaving basal HCN functions unaltered. In
 378 addition and in contrast to even the most selective blockers, it is selective for HCN and it
 379 does not interfere with other cAMP-modulated channels present in the SAN, such as L-
 380 type Ca²⁺ channels. Collectively, this makes TRIP8b_{nano} a promising tool in targeted
 381 therapeutic interventions.

382

383 **Materials and Methods**

384 **Key resources table**

Reagent type. Species	Designation	Source or Reference	Identifiers	Additional information
gene (human)	HCN1	Xention Ltd. (Cambridge, UK)	NM_021072.3	
gene (mouse)	HCN2	other	NM_008226.2	Laboratory of Steven A.

				Siegelbaum
gene (rabbit)	HCN4	PMID: 10212270	NM_001082707.1	
gene (mouse)	TRIP8b	other	NM_001163516.3	Laboratory of Steven A. Siegelbaum
strain, strain background (E. coli)	DH5 α	Thermo Fisher Scientific		
strain, strain background (E. coli)	Stbl2	Thermo Fisher Scientific		
strain, strain background (Mus musculus)	either male or female mice	The Jackson Laboratory	RRID: C57BL6/J	
strain, strain background (Oryctolagus cuniculus)	New Zealand white female rabbits	Envigo	RRID: HsdOkd:NZW	
cell line (human)	HEK 293T	ATCC	RRID: CRL- 3216 TM	Tested negative for mycoplasma
biological sample (Mus musculus)	Isolated adult Sinoatrial node (SAN) cardiomyocytes	PMID: 11557233		
biological sample (Oryctolagus cuniculus)	Isolated adult Sinoatrial node (SAN) cardiomyocytes	PMID: 2432247		
recombinant DNA reagent	pET-52b (plasmid)	EMD Millipore		
recombinant DNA reagent	modified pET- 24b (plasmid)	Laboratory of Daniel L. Minor, Jr.		
recombinant DNA reagent	pcDNA 3.1 (plasmid)	Clontech Laboratories		
recombinant DNA reagent	pCI (plasmid)	Promega		
recombinant DNA reagent	TRIP8nano (cDNA)	This paper		Made by PCR and cloning; see Constructs
recombinant DNA reagent	TRIP8nano (E240R) (cDNA)	This paper		Made by site- directed mutagenesis of TRIP8bna no wt; see Constructs

recombinant DNA reagent	TRIP8bnano (E241R) (cDNA)	This paper		Made by site-directed mutagenesis of TRIP8bna no wt; see Constructs
recombinant DNA reagent	TRIP8bnano (E264K) (cDNA)	This paper		Made by site-directed mutagenesis of TRIP8bna no wt; see Constructs
recombinant DNA reagent	(E265K) (cDNA)	This paper		Made by site-directed mutagenesis of TRIP8bna no wt; see Constructs
recombinant DNA reagent	TRIP8bnano (D252N) (cDNA)	This paper		Made by site-directed mutagenesis of TRIP8bna no wt; see Constructs
recombinant DNA reagent	TRIP8bcore (cDNA)	PMID: 25197093		
recombinant DNA reagent	human HCN2 CNBD (cDNA)	PMID: 25197093		
recombinant DNA reagent	human HCN2 CNBD (N547D) (cDNA)	This paper		Made by site-directed mutagenesis of human HCN2 CNBD wt; see Constructs
recombinant DNA reagent	human HCN2 CNBD (K665E) (cDNA)	This paper		Made by site-directed mutagenesis of human HCN2 CNBD wt; see Constructs
recombinant DNA reagent	human HCN2 CNBD (K666E) (cDNA)	This paper		Made by site-directed mutagenesis of human HCN2 CNBD wt; see Constructs

recombinant DNA reagent	human HCN2 CNBD (R650E) (cDNA)	This paper		Made by site-directed mutagenesis of human HCN2 CNBD wt; see Constructs
recombinant DNA reagent	human HCN1 (cDNA)	Xention Ltd. (Cambridge, UK)		
recombinant DNA reagent	TRIP8b (1a4) (cDNA)	This paper		Made by PCR and cloning, see Constructs
recombinant DNA reagent	mouse HCN2 (cDNA)	Laboratory of Steven A. Siegelbaum		
recombinant DNA reagent	rabbit HCN4 (cDNA)	PMID: 10212270		
recombinant DNA reagent	mouse HCN2 (N520D) (cDNA)	This paper		Made by site-directed mutagenesis of mouse HCN2 wt; see Constructs
sequence-based reagent	human HCN1 (R549E) (cDNA)	This paper		Made by site-directed mutagenesis of human HCN1 wt; see Constructs
peptide, recombinant protein	TAT-TRIP8b _{nano} (YGRKKRRQR RRG-NHSLEEEFERA KAAVESTEFW DKMQAEWEE MARRNWISEN)	CASLO ApS		
peptide, recombinant protein	TAT-(SCRAMBLED) TRIP8b _{nano} (YGRKKRRQR RRG-RNEAEAAEVA QKDMINERAR THEFEWESWE MWENLSESEFK)	CASLO ApS		

commercial assay or kit	QuikChange Lightning Site-Directed Mutagenesis Kit	Agilent		
commercial assay or kit	Thermo Scientific TurboFect Transfection Reagent	Thermo Fisher Scientific		
chemical compound, drug	Adenosine 3',5'-cyclic monophosphate (cAMP)	SIGMA		
software, algorithm	Clampfit 10.5/10.7	Molecular Devices	RRID:SCR_011323	
software, algorithm	CYANA-2.1	L. A. Systems, Inc.		
software, algorithm	AMBER 12.0	http://pyenmr.cem.unifi.it/access/index/amps-nmr		
software, algorithm	HADDOCK2.2	www.wenmr.eu		

385

386 **Constructs**

387 The cDNA fragment encoding residues 235 – 275 (TRIP8b_{nano}) of mouse TRIP8b (splice
388 variant 1a4) was cloned into pET-52b (EMD Millipore) downstream of a Strep (II) tag
389 sequence, while the cDNA fragment encoding residues 521–672 of human HCN2 (HCN2
390 CNBD) was cloned, in a previous study, into a modified pET-24b downstream of a double
391 His₆-maltose-binding protein (MBP) (Saponaro et al., 2014). The cDNA encoding full-
392 length human HCN1 channel and mouse TRIP8b (1a4) were cloned into the mammalian
393 expression vector pcDNA 3.1 (Clontech Laboratories), while mouse HCN2 channel and
394 rabbit HCN4 channel were cloned into the mammalian expression vector pCI (Promega).
395 Mutations were generated by site-directed mutagenesis (QuikChange site-directed
396 mutagenesis kit; Agilent Technologies) and confirmed by sequencing.

397 **Preparation of proteins**

398 The HCN2 CNBD WT and mutant proteins, as well as the TRIP8b_{core} and TRIP8b_{nano}
399 proteins (WT and mutants) were produced and purified following the procedure previously
400 described (Saponaro et al., 2014).

401 **Structure calculation of the cAMP-free human HCN2 CNBD in complex with**
402 **TRIP8b_{nano} and vice versa**

403 NMR experiments were acquired on Bruker Avance III 950, 700 and 500 MHz NMR
404 spectrometers equipped with a TXI-cryoprobe at 298 K. The acquired triple resonance
405 NMR experiments for the assignment of backbone resonances of cAMP-free HCN2 CNBD
406 (CNBD hereafter) in complex with TRIP8b_{nano} and vice versa are summarized in *Figure 3-*
407 *source data 1*. ¹⁵N, ¹³C', ¹³C_α, ¹³C_β, and H_α chemical shifts were used to derive φ and ψ
408 dihedral angles by TALOS+ program (Cornilescu, Delaglio, & Bax, 1999) for both CNBD
409 and TRIP8b_{nano}. For TRIP8b_{nano}, CYANA-2.1 structure calculation (Guntert & Buchner,
410 2015) was performed using 68 φ and ψ dihedral angles and 40 backbone hydrogen bonds
411 as input. For CNBD, CYANA-2.1 structure calculation was performed using 108 φ and ψ
412 dihedral angles, combined with the NOEs obtained in our previous determination of the
413 cAMP-free form of the CNBD (Saponaro et al., 2014) for those regions not affected by the
414 interaction with TRIP8b_{nano}. The 10 conformers of TRIP8b_{nano} and CNBD with the lowest
415 residual target function values were subjected to restrained energy minimization with
416 AMBER 12.0 (Case et al., 2012) (<http://pyenmr.cerm.unifi.it/access/index/amps-nmr>) and
417 used as input in docking calculations.

418 **Docking calculations**

419 Docking calculations were performed with HADDOCK2.2 implemented in the
420 WeNMR/West-Life GRID-enabled web portal (www.wenmr.eu). The docking calculations
421 are driven by ambiguous interaction restraints (AIRs) between all residues involved in the
422 intermolecular interactions (Dominguez, Boelens, & Bonvin, 2003). Active residues of the
423 CNBD were defined as the surface exposed residues (at least 50% of solvent
424 accessibility), which show chemical shift perturbation upon TRIP8b_{nano} binding.

425 The assignment of the CNBD bound to TRIP8b_{nano} allowed to highlight the residues of
426 CNBD whose backbone featured appreciable Combined Chemical Shift Perturbation
427 (CSP) (*Figure 3-figure supplement 1*). The combined CSP (Δ_{HN}) is given by the equation
428 $\Delta_{HN} = \{((H_{Nfree} - H_{Nbound})^2 + ((N_{free} - N_{bound})/5)^2)/2\}^{1/2}$ (Garrett, Seok, Peterkofsky, Clore, &
429 Gronenborn, 1997).

430 Passive residues of CNBD were defined as the residues close in space to active residues
431 and with at least 50% solvent accessibility.

432 In the case of TRIP8b_{nano}, the conserved stretch E₂₃₉-E₂₄₃, located in helix N, was defined
433 as active region in a first docking calculation, while all the other solvent accessible
434 residues of the peptide were defined as passive. This docking calculation generated
435 several clusters. A post-docking filter step allowed us to select those clusters having an
436 orientation of TRIP8b_{nano} bound to CNBD in agreement with a DEER study on the CNBD -
437 TRIP8b_{nano} interaction (Deberg et al., 2015). The selected clusters grouped in two classes
438 on the basis of the orientation of helix N of TRIP8b_{nano} (N) relative to CNBD (*Figure 3-*
439 *figure supplement 2*). A second docking calculation was subsequently performed
440 introducing also residues E₂₆₄-E₂₆₅, located in helix C of TRIP8b_{nano} as active residues. The
441 active residues for CNBD were the same used for the first calculation. For this second
442 HADDOCK calculation 14 clusters were obtained and ranked according to their
443 HADDOCK score. Among them only four clusters showed both an orientation of
444 TRIP8b_{nano} bound to CNBD in agreement with the DEER study (Deberg et al., 2015) and
445 the involvement of E₂₃₉-E₂₄₃ stretch of TRIP8b_{nano} in the binding to CNBD. These clusters
446 were manually analyzed and subjected to a per-cluster re-analysis following the protocol
447 reported in <http://www.bonvinlab.org/software/haddock2.2/analysis/#reanal>. From this
448 analysis, it resulted that the top-ranking cluster, i.e. the one with the best energetic and
449 scoring functions, has a conformation in agreement with mutagenesis experiments (*Figure*
450 *3-figure supplement 3*). Energy parameters (van der Waals energy, electrostatic energy,
451 desolvation energy, and the penalty energy due to violation of restraints) for this complex
452 model are reported in *Figure 3-source data 2*.

453 Both docking calculations were performed using 10 NMR conformers of both the CNBD
454 and the TRIP8b_{nano} structures calculated as described above. In the TRIP8b_{nano} structures
455 the unfolded N- and C-terminal regions were removed, while in the CNBD structures only
456 the unfolded N-terminal region was removed. This is because the C-terminal region of the
457 CNBD is known to comprise residues involved in TRIP8b_{nano} binding (Saponaro et al.,
458 2014). Flexible regions of the proteins were defined based on the active and passive
459 residues plus two preceding and following residues. The residue solvent accessibility was
460 calculated with the program NACCESS (Hu et al., 2013). In the initial rigid body docking
461 calculation phase, 5000 structures of the complex were generated, and the best 400 in
462 terms of total intermolecular energy were further submitted to the semi-flexible simulated
463 annealing and a final refinement in water. Random removal of the restraints was turned
464 off. The number of flexible refinement steps was increased from the default value of
465 500/500/1000/1000 to 2000/2000/2000/4000. The final 400 structures were then clustered

466 using a cutoff of 5.0 Å of RMSD to take into consideration the smaller size of protein-
467 peptide interface.

468 **Electrophysiology of HEK 293T cells**

469 HEK 293T cells were cultured in Dulbecco's modified Eagle's medium (Euroclone)
470 supplemented with 10% fetal bovine serum (Euroclone), 1% Pen Strep (100 U/mL of
471 penicillin and 100 µg/ml of streptomycin), and stored in a 37°C humidified incubator with
472 5% CO₂. The plasmid containing cDNA of wild-type and mutant HCN1, HCN2 and HCN4
473 channels (1 µg) was co-transfected for transient expression into HEK 293T cells with a
474 plasmid containing cDNA of Green Fluorescent Protein (GFP) (1.3 µg). For co-expression
475 with TRIP8b (1a-4), HEK 293T cells were transiently transfected with wild-type (wt) and/or
476 mutant human HCN1 cDNA (1 µg), wt TRIP8b (1a-4) cDNA (1 µg) and cDNA of Green
477 Fluorescent Protein (GFP) (0.3 µg).

478 One day after transfection, GFP-expressing cells were selected for patch-clamp
479 experiments in whole-cell configuration. The experiments were conducted at R.T. The
480 pipette solution in whole cell experiments contained: 10 mM NaCl, 130 mM KCl, 1 mM
481 egtazic acid (EGTA), 0.5 mM MgCl₂, 2 mM ATP (Mg salt) and 5 mM HEPES–KOH buffer
482 (pH 7.4). The extracellular bath solution contained 110 mM NaCl, 30 mM KCl, 1.8 mM
483 CaCl₂, 0.5 mM MgCl₂ and 5 mM HEPES–KOH buffer (pH 7.4).

484 TRIP8b_{nano} was added (10 µM) to the pipette solution. cAMP was added at different
485 concentration to the pipette solution depending on the HCN isoform used: 0 µM for HCN1,
486 5 µM for HCN2 and 1 µM for HCN4.

487 Whole-cell measurements of HCN channels were performed using the following voltage
488 clamp protocol depending on the HCN isoform measured: for HCN1, holding potential was
489 –30 mV (1s), with steps from –20 mV to –120 mV (10 mV interval, 3.5 s) and tail currents
490 recorded at –40mV (3 s); for HCN2, holding potential was –30 mV (1 s), with steps from –
491 40 mV to –130 mV (10 mV interval, 5 s) and tail currents recorded at -40mV (5 s); for
492 HCN4, holding potential was –30 mV (1s), steps from –30 mV to –165 mV (15 mV interval,
493 4.5 s) and tail currents were recorded at -40mV (5 s). Current voltage relations and
494 activation curves were obtained by the above activation and deactivation protocols and
495 analysed by the Boltzmann equation, see data analysis.

496

497 **Isolation and electrophysiology of rabbit sinoatrial node cells**

498 Animal protocols conformed to the guidelines of the care and use of laboratory animals
499 established by Italian and European Directives (D. Lgs n° 2014/26, 2010/63/UE). New
500 Zealand white female rabbits (0.8–1.2 kg) were anesthetized (xylazine 5mg/Kg, i.m.), and
501 euthanized with an overdose of sodium thiopental (i.v.); hearts were quickly removed, and
502 the SAN region was isolated and cut in small pieces. Single SAN cardiomyocytes were
503 isolated following an enzymatic and mechanical procedure as previously described
504 (DiFrancesco, Ferroni, Mazzanti, & Tromba, 1986). Following isolation, cells were
505 maintained at 4 °C in Tyrode solution: 140 mM NaCl, 5.4 mM KCl, 1.8 mM CaCl₂, 1 mM
506 MgCl₂, 5.5 mM D-glucose, 5 mM HEPES-NaOH (pH 7.4).

507 For patch clamp experiments cells were placed in a chamber on an inverted microscope
508 and experiments were performed in the whole-cell configuration at 35 ± 0.5 °C. The pipette
509 solution contained: 10 mM NaCl, 130 mM KCl, 1 mM egtazic acid (EGTA), 0.5 mM MgCl₂,
510 and 5 mM HEPES–KOH buffer (pH 7.2). The I_f current was recorded from single cells
511 superfused with Tyrode solution with 1 mM BaCl₂, and 2 mM MnCl₂.

512 I_f activation curves were obtained using a two-step protocol in which test voltage steps
513 (from -30 to -120 mV, 15 mV interval) were applied from a holding potential of -30 mV and
514 were followed by a step to -125 mV. Test steps had variable durations so as to reach
515 steady –state activation at all voltages. Analysis was performed with the Boltzmann
516 equation (see data analysis).

517 In current-clamp studies, spontaneous action potentials were recorded from single cells
518 superfused with Tyrode solution, and rate was measured from the interval between
519 successive action potential. When indicated cAMP (1 μM) and/or nanoTRIP8b (10 μM)
520 were added to the pipette solution.

521 **Isolation and electrophysiology of mouse sinoatrial node cells**

522 Mice were killed by cervical dislocation under general anesthesia consisting of 0.01 mg/g
523 xylazine (2% Rompun; Bayer AG), 0.1 mg/g ketamine (Imalgène; Merial) and 0.04mg/g of
524 Na-pentobarbital (Euthanasol VET, Laboratoire TVM, Lempdes, France), and beating
525 hearts were quickly removed. The SAN region was excised in warmed (35°C) Tyrode's
526 solution containing: 140 mM NaCl, 5.4 mM KCl, 1.8 mM CaCl₂, 1 mM MgCl₂, 1 mM Hepes-
527 NaOH (pH = 7.4), and 5.5 mM D-glucose and cut in strips. Strips were then transferred
528 into a "low-Ca²⁺-low-Mg²⁺" solution containing: 140 mM NaCl; 5.4 mM KCl, 0.5 mM MgCl₂,

529 0.2 mM CaCl₂, 1.2 mM KH₂PO₄, 50 mM taurine, 5.5 mM D-glucose, 1 mg/ml bovine serum
530 albumin (BSA), 5 mM Hepes-NaOH (pH = 6.9).

531 Tissue was digested by adding Liberase TH (0.15 mg/ml, Roche Diagnostics GmbH,
532 Mannheim, Germany), elastase (1.9 U/ml, Worthington, Lakewood, USA). Digestion was
533 carried out for a variable time of 15–18 minutes at 35°C. Tissue strips were then washed
534 and transferred into a modified “Kraftbrühe” (KB) medium containing: 70 mM L-glutamic
535 acid, 20 mM KCl, 80 mM KOH, (±) 10 mM D- b-OH-butyric acid; 10 mM KH₂PO₄, 10 mM
536 taurine, 1mg/ml BSA and 10 mM Hepes-KOH (pH = 7.4).

537 Single SAN cells were isolated by manual agitation in KB solution at 35°C for 30–50
538 seconds.

539 Cellular automaticity was recovered by re-adapting the cells to a physiological extracellular
540 Ca²⁺ concentration by addition of a solution containing: 10 mM NaCl, 1.8 mM CaCl₂ and
541 normal Tyrode solution containing BSA (1 mg/ml). The final storage solution contained:
542 100 mM NaCl, 35 mM KCl, 1.3 mM CaCl₂, 0.7 mM MgCl₂, 14 mM L-glutamic acid, (±) 2
543 mM D-b-OH-butyric acid, 2 mM KH₂PO₄, 2 mM taurine, 1 mg/ml BSA, (pH = 7.4). Cells
544 were then stored at room temperature until use. All chemicals were from SIGMA (St
545 Quentin Fallavier, France).

546 For electrophysiological recording, SAN cells in the storage solution were harvested in
547 special custom-made recording plexiglas chambers with glass bottoms for proper cell
548 attachment and mounted on the stage of an inverted microscope (Olympus IX71) and
549 perfused with normal Tyrode solution. The recording temperature was 36°C. We used the
550 whole-cell variation of the patch-clamp technique to record cellular ionic currents, by
551 employing a Multiclamp 700B (Axon Instruments Inc., Foster USA) patch clamp amplifier.
552 Recording electrodes were fabricated from borosilicate glass, by employing a WZ DMZ-
553 Universal microelectrode puller (Zeitz-Instruments Vertriebs GmbH, Martinsried,
554 Germany).

555 I_f was recorded under standard whole-cell configuration during perfusion of standard
556 Tyrode's containing 2 mM BaCl₂ to block I_{K1}. Patch-clamp pipettes were filled with an
557 intracellular solution containing: 130 mM KCl, 10 mM NaCl, 1 mM EGTA, 0.5 mM MgCl₂
558 and 5 mM HEPES (pH 7.2).

559 For recording of L-type Ca²⁺ currents, pipette solution contained: 125 mM CsOH, 20 mM
560 tetraethylammonium chloride (TEA-Cl), 1.2 mM CaCl₂, 5 mM Mg-ATP, 0.1 mM Li₂-GTP, 5

561 mM EGTA and 10 mM HEPES (pH 7.2 with aspartate). 30 μ M TTX (Latoxan, Portes lès
562 Valence, France) to block INa was added to external solution containing: 135 mM
563 tetraethylammonium chloride (TEA-Cl), 4 mM CaCl₂, 10 mM 4-amino-pyridine, 1 mM
564 MgCl₂, 10 mM HEPES and 1 mg/ml Glucose (pH 7.4 with TEA-OH).

565 Electrodes had a resistance of about 3 M Ω . Seal resistances were in the range of 2–5 G Ω .
566 10 μ M TRIPb_{8nano} was added to pipette solution. 10 μ M TAT-TRIPb_{8nano} was added in cell
567 storage solution for at least 30 min before patch clamp recording.

568 **TAT-peptides**

569

570 TAT-TRIPb_{8nano} (**YGRKKRRQRRRGG**-NHSLEEEFERAKAAVESTEFWDKMQAEWEEMARRNWISEN,
571 TAT sequence is shown in bold type) and TAT-(SCRAMBLED)TRIPb_{8nano}
572 (**YGRKKRRQRRRGG**-RNEAEAAEVAQKDMINERARTHEFEWESWEMWENLSESEFK, TAT sequence is
573 shown in bold type) were purchased from CASLO ApS. TAT-peptides were dissolved in
574 Milliq water (1.5 mM) and added to the petri dish at the final concentration (10 μ M) 30
575 minutes before current recordings. During the patch clamp experiments, cells were
576 perfused with standard Tyrode with 2 mM BaCl₂ (see above) without the peptides.
577 Recordings from the same petri dish were performed over a time window of 10 to 60
578 minutes in peptide-free solution

579

580 **Data analysis**

581 Data were acquired at 1 kHz using an Axopatch 200B amplifier and pClamp10.5 or 10.7
582 software (Axon Instruments). Data were analyzed off-line using Clampfit 10.5 or 10.7
583 (Molecular Devices) and Origin 2015 or 16 (OriginLab Corp., Northampton MA). Activation
584 curves were analysed by the Boltzmann equation, $y=1/\{1+\exp[(V-V_{1/2})/s]\}$, where y is
585 fractional activation, V is voltage, V_{1/2} half-activation voltage, and s the inverse slope factor
586 (mV) (DiFrancesco, 1999). Mean activation curves were obtained by fitting individual
587 curves from each cell to the Boltzmann equation and then averaging all curves obtained.
588 Activation time constants (τ_{on}) were obtained by fitting a single exponential function,

589 $I=I_0 \exp(-t/\tau)$ to current traces recorded at the indicated voltages.

590 **Ethics statement**

591 Experiments on rabbit SAN cells were performed using left-over cells obtained during
592 experiments approved by the Animal Welfare Body of the University of Milan and by the
593 Italian Ministry of Health (license n.1127/2015-PR). Animal procedures were conformed to
594 the guidelines of the care and use of laboratory animals established by Italian and
595 European Directives (D. Lgs n° 2014/26, 2010/63/UE).

596 Mouse primary pacemaker cells were isolated from adult C5B6/J mice as previously
597 described (Mangoni and Nargeot, Cardiovasc Res 2001), in accordance with the Guide for
598 the Care and Use of Laboratory Animals (eighth edition, 2011), published by the US
599 National Institute of Health and European directives (2010/63/EU). The protocol was
600 approved by the ethical committee of the University of Montpellier and the French Ministry
601 of Agriculture (protocol N°: 2017010310594939).

602

603

604 **Acknowledgements**

605 This work has been supported by Fondazione CARIPLO grant 2014-0796 to A.M., B.S and
606 L.B., by 2016 Schaefer Research Scholars Program of Columbia University to A.M., by
607 European Research Council (ERC) 2015 Advanced Grant 495 (AdG) n. 695078 noMAGIC
608 to A.M. and G.T., by National Institutes for Health Grant R01 NS036658 to B.S., by
609 Instruct-ERIC and national member subscriptions to L.B, and by Accademia Nazionale dei
610 Lincei (Giuseppe Levi foundation) to A.S. We specially thank the EU ESFRI Instruct Core
611 Centre CERM-Italy.

612

613 **Conflict of interest:** none

614

615 **References**

- 616
617 Bankston, J. R., DeBerg, H. A., Stoll, S., & Zagotta, W. N. (2017). Mechanism for the inhibition of the cAMP
618 dependence of HCN ion channels by the auxiliary subunit TRIP8b. *The Journal of Biological Chemistry*.
619 Retrieved from <https://doi.org/10.1074/jbc.M117.800722>
- 620 Case DA, et al. (2012) AMBER 12 (University of California, San Francisco)
- 621 Chen, S., Wang, J., & Siegelbaum, S. A. (2001). Properties of Hyperpolarization-Activated Pacemaker
622 Current Defined by Coassembly of Hcn1 and Hcn2 Subunits and Basal Modulation by Cyclic
623 Nucleotide. *The Journal of General Physiology*, 117(5), 491–504. Retrieved from
624 <https://doi.org/10.1085/jgp.117.5.491>
- 625 Cornilescu, G., Delaglio, F., & Bax, A. (1999). Protein backbone angle restraints from searching a database
626 for chemical shift and sequence homology. *Journal of Biomolecular NMR*, 13(3), 289–302.
- 627 Craven, K. B., & Zagotta, W. N. (2004). Salt bridges and gating in the COOH-terminal region of HCN2 and
628 CNGA1 channels. *The Journal of General Physiology*, 124(6), 663–677. Retrieved from
629 <https://doi.org/10.1085/jgp.200409178>
- 630 Deberg, H. A., Bankston, J. R., Rosenbaum, J. C., Brzovic, P. S., Zagotta, W. N., & Stoll, S. (2015). Structural
631 mechanism for the regulation of HCN ion channels by the accessory protein TRIP8b. *Structure*, 23(4),
632 734–744. Retrieved from <https://doi.org/10.1016/j.str.2015.02.007>
- 633 DiFrancesco, D. (1993). Pacemaker mechanisms in cardiac tissue. *Annual Review of Physiology*, 55, 455–
634 472. Retrieved from <https://doi.org/10.1146/annurev.physiol.55.1.455>
- 635 DiFrancesco, D. (1999). Dual allosteric modulation of pacemaker (f) channels by cAMP and voltage in rabbit
636 SA node. *The Journal of Physiology*, 515 (Pt 2, 367–376.
- 637 DiFrancesco, D., Ducouret, P., & Robinson, R. B. (1989). Muscarinic modulation of cardiac rate at low
638 acetylcholine concentrations. *Science*, 243(4891), 669–671. Retrieved from
639 <https://doi.org/10.1126/science.2916119>
- 640 DiFrancesco, D., Ferroni, A., Mazzanti, M., & Tromba, C. (1986). Properties of the hyperpolarizing-activated
641 current (if) in cells isolated from the rabbit sino-atrial node. *The Journal of Physiology*, 377, 61–88.
- 642 DiFrancesco, D., & Tortora, P. (1991). Direct activation of cardiac pacemaker channels by intracellular cyclic
643 AMP. *Nature*, 351(6322), 145–147. Retrieved from <https://doi.org/10.1038/351145a0>
- 644 Dominguez, C., Boelens, R., & Bonvin, A. M. J. J. (2003). HADDOCK: a protein-protein docking approach
645 based on biochemical or biophysical information. *Journal of the American Chemical Society*, 125(7),
646 1731–1737. Retrieved from <https://doi.org/10.1021/ja026939x>
- 647 Dyson, H. J., & Wright, P. E. (2004). Unfolded proteins and protein folding studied by NMR. *Chemical*
648 *Reviews*, 104(8), 3607–3622. Retrieved from <https://doi.org/10.1021/cr030403s>
- 649 Emery, E. C., Young, G. T., & McNaughton, P. A. (2012). HCN2 ion channels: An emerging role as the
650 pacemakers of pain. *Trends in Pharmacological Sciences*. Retrieved from
651 <https://doi.org/10.1016/j.tips.2012.04.004>
- 652 Fosgerau, K., & Hoffmann, T. (2015). Peptide therapeutics: current status and future directions. *Drug*
653 *Discovery Today*, 20(1), 122–128. Retrieved from <https://doi.org/10.1016/j.drudis.2014.10.003>
- 654 Garrett, D. S., Seok, Y. J., Peterkofsky, A., Clore, G. M., & Gronenborn, A. M. (1997). Identification by NMR
655 of the binding surface for the histidine-containing phosphocarrier protein HPr on the N-terminal
656 domain of enzyme I of the Escherichia coli phosphotransferase system. *Biochemistry*, 36(15), 4393–
657 4398. Retrieved from <https://doi.org/10.1021/bi970221q>
- 658 Guidotti, G., Brambilla, L., & Rossi, D. (2017). Cell-Penetrating Peptides: From Basic Research to Clinics.

- 659 *Trends in Pharmacological Sciences*, 38(4), 406–424. Retrieved from
660 <https://doi.org/10.1016/j.tips.2017.01.003>
- 661 Guntert, P., & Buchner, L. (2015). Combined automated NOE assignment and structure calculation with
662 CYANA. *Journal of Biomolecular NMR*, 62(4), 453–471. Retrieved from
663 <https://doi.org/10.1007/s10858-015-9924-9>
- 664 Han, Y., Noam, Y., Lewis, A. S., Gallagher, J. J., Wadman, W. J., Baram, T. Z., & Chetkovich, D. M. (2011).
665 Trafficking and gating of hyperpolarization-activated cyclic nucleotide-gated channels are regulated by
666 interaction with tetratricopeptide repeat-containing Rab8b-interacting protein (TRIP8b) and cyclic
667 AMP at distinct sites. *The Journal of Biological Chemistry*, 286(23), 20823–20834. Retrieved from
668 <https://doi.org/10.1074/jbc.M111.236125>
- 669 Henninot, A., Collins, J. C., & Nuss, J. M. (2017). The Current State of Peptide Drug Discovery: Back to the
670 Future? *Journal of Medicinal Chemistry*. Retrieved from
671 <https://doi.org/10.1021/acs.jmedchem.7b00318>
- 672 Herce, H. D., Garcia, A. E., & Cardoso, M. C. (2014). Fundamental molecular mechanism for the cellular
673 uptake of guanidinium-rich molecules. *Journal of the American Chemical Society*, 136(50), 17459–
674 17467. Retrieved from <https://doi.org/10.1021/ja507790z>
- 675 Herrmann, S., Rajab, H., Christ, I., Schirdewahn, C., Hofler, D., Fischer, M. J. M., ... Ludwig, A. (2017). Protein
676 kinase A regulates inflammatory pain sensitization by modulating HCN2 channel activity in nociceptive
677 sensory neurons. *Pain*, 158(10), 2012–2024. Retrieved from
678 <https://doi.org/10.1097/j.pain.0000000000001005>
- 679 Hu, L., Santoro, B., Saponaro, A., Liu, H., Moroni, A., & Siegelbaum, S. (2013). Binding of the auxiliary
680 subunit TRIP8b to HCN channels shifts the mode of action of cAMP. *The Journal of General Physiology*,
681 142(6), 599–612. Retrieved from <https://doi.org/10.1085/jgp.201311013>
- 682 Kristensen, M., Birch, D., & Morck Nielsen, H. (2016). Applications and Challenges for Use of Cell-
683 Penetrating Peptides as Delivery Vectors for Peptide and Protein Cargos. *International Journal of*
684 *Molecular Sciences*, 17(2). Retrieved from <https://doi.org/10.3390/ijms17020185>
- 685 Lee, C.-H., & MacKinnon, R. (2017). Structures of the Human HCN1 Hyperpolarization-Activated Channel.
686 *Cell*, 168(1–2), 111–120.e11. Retrieved from <https://doi.org/10.1016/j.cell.2016.12.023>
- 687 Lolicato, M., Nardini, M., Gazzarrini, S., Moller, S., Bertinetti, D., Herberg, F. W., ... Moroni, A. (2011).
688 Tetramerization dynamics of C-terminal domain underlies isoform-specific cAMP gating in
689 hyperpolarization-activated cyclic nucleotide-gated channels. *The Journal of Biological Chemistry*,
690 286(52), 44811–44820. Retrieved from <https://doi.org/10.1074/jbc.M111.297606>
- 691 Lyman, K. A., Han, Y., Heuermann, R. J., Cheng, X., Kurz, J. E., Lyman, R. E., ... Chetkovich, D. M. (2017).
692 Allosteric interaction between two binding sites in the ion channel subunit TRIP8b confers binding specificity to
693 HCN channels. *The Journal of Biological Chemistry*. Retrieved from
694 <https://doi.org/10.1074/jbc.M117.802256>
- 695 Puljung, M. C., & Zagotta, W. N. (2013). A secondary structural transition in the C-helix promotes gating of
696 cyclic nucleotide-regulated ion channels. *Journal of Biological Chemistry*, 288(18), 12944–12956.
697 Retrieved from <https://doi.org/10.1074/jbc.M113.464123>
- 698 Robinson, R. B., & Siegelbaum, S. A. (2003). Hyperpolarization-Activated Cation Currents: From Molecules
699 to Physiological Function. *Annual Review of Physiology*, 65(1), 453–480. Retrieved from
700 <https://doi.org/10.1146/annurev.physiol.65.092101.142734>
- 701 Santoro, B., Hu, L., Liu, H., Saponaro, A., Pian, P., Piskorowski, R. A., ... Siegelbaum, S. A. (2011). TRIP8b
702 Regulates HCN1 Channel Trafficking and Gating through Two Distinct C-Terminal Interaction Sites.
703 *Journal of Neuroscience*, 31(11), 4074–4086. Retrieved from

- 704 <https://doi.org/10.1523/JNEUROSCI.5707-10.2011>
- 705 Santoro, B., Piskorowski, R. A., Pian, P., Hu, L., Liu, H., & Siegelbaum, S. A. (2009). TRIP8b Splice Variants
706 Form a Family of Auxiliary Subunits that Regulate Gating and Trafficking of HCN Channels in the Brain.
707 *Neuron*, 62(6), 802–813. Retrieved from <https://doi.org/10.1016/j.neuron.2009.05.009>
- 708 Saponaro, A., Pauleta, S. R., Cantini, F., Matzapetakis, M., Hammann, C., Donadoni, C., ... Moroni, A. (2014).
709 Structural basis for the mutual antagonism of cAMP and TRIP8b in regulating HCN channel function.
710 *Proceedings of the National Academy of Sciences of the United States of America*, 111(40), 14577–
711 14582. Retrieved from <https://doi.org/10.1073/pnas.1410389111>
- 712 Wainger, B. J., DeGennaro, M., Santoro, B., Siegelbaum, S. A., & Tibbs, G. R. (2001). Molecular mechanism
713 of cAMP modulation of HCN pacemaker channels. *Nature*, 411(6839), 805–810. Retrieved from
714 <https://doi.org/10.1038/35081088>
- 715 Weissgraeber, S., Saponaro, A., Thiel, G., & Hamacher, K. (2017). A reduced mechanical model for cAMP-
716 modulated gating in HCN channels. *Scientific Reports*, 7, 40168. Retrieved from
717 <https://doi.org/10.1038/srep40168>
- 718 Zagotta, W. N., Olivier, N. B., Black, K. D., Young, E. C., Olson, R., & Gouaux, E. (2003). Structural basis for
719 modulation and agonist specificity of HCN pacemaker channels. *Nature*, 425(6954), 200–205.
720 Retrieved from <https://doi.org/10.1038/nature01922>
- 721 Zhou, L., & Siegelbaum, S. A. (2007). Gating of HCN channels by cyclic nucleotides: residue contacts that
722 underlie ligand binding, selectivity, and efficacy. *Structure (London, England : 1993)*, 15(6), 655–670.
723 Retrieved from <https://doi.org/10.1016/j.str.2007.04.012>
- 724 Zolles, G., Wenzel, D., Bildl, W., Schulte, U., Hofmann, A., Muller, C. S., ... Klocker, N. (2009). Association
725 with the auxiliary subunit PEX5R/Trip8b controls responsiveness of HCN channels to cAMP and
726 adrenergic stimulation. *Neuron*, 62(6), 814–825. Retrieved from
727 <https://doi.org/10.1016/j.neuron.2009.05.008>

728

729

730 **Figure 1.** Functional and structural characterization of TRIP8b_{nano}. **(A)** Primary sequence
731 of TRIP8b_{nano}. Amino acid numbering refers to full length mouse TRIP8b (1a4). **(B)** Binding
732 of TRIP8b_{core} and TRIP8b_{nano} to purified His₆-MBP-CNBD measured by Isothermal titration
733 calorimetry (ITC). Upper panel, heat changes ($\mu\text{cal/sec}$) during successive injections of 8
734 μL of the corresponding TRIP8b peptide (200 μM) into the chamber containing His₆-MBP-
735 CNBD (20 μM). Lower panel, binding curve obtained from data displayed in the upper
736 panel. The peaks were integrated, normalized to TRIP8b peptide concentration, and
737 plotted against the molar ratio (TRIP8b peptide / His₆-MBP-CNBD). Solid line represents a
738 nonlinear least-squares fit to a single-site binding model, yielding, in the present examples,
739 a $K_D = 1.2 \pm 0.1 \mu\text{M}$ for TRIP8b_{core} and $K_D = 1.4 \pm 0.1 \mu\text{M}$ for TRIP8b_{nano}. **(C)** Evidence for
740 TRIP8b_{nano} folding upon CNBD binding based on the superimposition of the [¹H, ¹⁵N]
741 heteronuclear single quantum coherence (HSQC) NMR spectrum of CNBD-free
742 TRIP8b_{nano} (black) and CNBD-bound TRIP8b_{nano} (red). The latter experiment was

743 performed at the molar ratio ($[\text{CNBD}]/[\text{TRIP8b}_{\text{nano}}] = 3$). The backbone amide (HN) signals
744 of the residues of CNBD-bound $\text{TRIP8b}_{\text{nano}}$ are labelled in red. **(D)** (Top) Ribbon
745 representation of the 10 lowest energy conformers of $\text{TRIP8b}_{\text{nano}}$ bound to CNBD used for
746 *in silico* modelling of CNBD $\text{TRIP8b}_{\text{nano}}$ complex. The unfolded regions at the N- and C-
747 termini of the construct (residues 235–237 and 270 – 275) are omitted for clarity. (Bottom)
748 Chemical Shift Index (CSI, calculated using TALOS+) plotted as a function of the residue
749 number of $\text{TRIP8b}_{\text{nano}}$ bound to CNBD. Positive values represent helical propensity.

750

751

752

753 **Figure 2.** NMR structure of CNBD bound to $\text{TRIP8b}_{\text{nano}}$. **(A)** (Top) comparison of
754 secondary structure elements of cAMP-free CNBD (Saponaro et al., 2014), cAMP-bound
755 CNBD (Zagotta et al., 2003) and cAMP-free CNBD bound to $\text{TRIP8b}_{\text{nano}}$ (this study).
756 Secondary structure elements are indicated by arrows (β -strands) and cylinders (α -
757 helices) and labelled. The loop between β_6 and β_7 constitutes the Phosphate Binding
758 Cassette (PBC). The elements that fold upon binding of cAMP and $\text{TRIP8b}_{\text{nano}}$ are shown
759 in red. (Bottom) Chemical Shift Index (CSI, calculated using TALOS+) plotted as a function
760 of the residue number of CNBD bound to $\text{TRIP8b}_{\text{nano}}$. Positive values represent helical
761 propensity, while negative values represent strands. **(B)** Ribbon representation of the 10
762 lowest energy conformers of CNBD bound to $\text{TRIP8b}_{\text{nano}}$ used for *in silico* modelling of
763 CNBD - $\text{TRIP8b}_{\text{nano}}$ complex. Secondary structure elements are coloured in light gray and
764 labelled. Loop regions are coloured in dark gray. The distal region of the C-helix (residues
765 657-662), which is unfolded in the free form of the CNBD (Saponaro *et al*, 2014) and folds
766 upon $\text{TRIP8b}_{\text{nano}}$ binding, is coloured in red. The unfolded regions at the N- and C-termini
767 of the construct (residues 521–532 and 663 – 672 respectively) are omitted for clarity.

768

769 **Figure 3.** Structural model of CNBD – $\text{TRIP8b}_{\text{nano}}$ complex. **(A)** Ribbon representation of
770 the complex where CNBD is in gray and $\text{TRIP8b}_{\text{nano}}$ is in orange. Helix N (N) and helix C
771 (C) of $\text{TRIP8b}_{\text{nano}}$ are labelled. C-helix of CNBD (αC) is labelled, while N-bundle loop is
772 coloured in yellow. Positively charged residues of C-helix CNBD (blue) and negatively
773 charged residues of $\text{TRIP8b}_{\text{nano}}$ (red) involved in salt bridges are shown as sticks and
774 labelled. N_{547} of the N-bundle loop (yellow) and D_{252} of $\text{TRIP8b}_{\text{nano}}$ (orange) are shown as

775 sticks and labelled. **(B)** Close view of K₆₆₅ and K₆₆₆ of CNBD that interact respectively with
776 E₂₆₅ and E₂₆₄ of TRIP8b_{nano}. C-helix (α C) of CNBD, and Helix C (C) of TRIP8b_{nano} are
777 labelled. **(C)** Close view of R₆₅₀ of CNBD that is positioned between E₂₄₀ and E₂₄₁ of
778 TRIP8b_{nano}. C-helix (α C) of CNBD, and Helix N (N) of TRIP8b_{nano} are labelled. **(D)** Close
779 view of N₅₄₇ of N-bundle loop that forms a hydrogen bond (red dashed line) with D₂₅₂ of
780 TRIP8b_{nano}. Helix E' (α E') and C-helix (α C) of CNBD, and Helix N (N) of TRIP8b_{nano} are
781 labelled.

782

783 **Figure 4.** TRIP8b_{nano} abolishes cAMP effect on HCN channel gating. **(A)** Representative
784 whole-cell HCN4, HCN2 and HCN1 currents recorded, at the indicated voltages, with
785 control solution or with cAMP (1 μ M for HCN4 and 5 μ M for HCN2) or cAMP + 10 μ M
786 TRIP8b_{nano} in the patch pipette (for HCN1 we added only 10 μ M TRIP8b_{nano}). **(B)** Mean
787 activation curves measured from HCN4, HCN2 and HCN1 in control solution (open
788 circles), cAMP (filled circles), cAMP + TRIP8b_{nano}, or TRIP8b_{nano} only in the case of
789 HCN1 (filled triangles). Solid and dashed lines indicate Boltzmann fitting to the data (see
790 Material and Methods). **(C)** Half activation potential ($V_{1/2}$) values of HCN4 (blue), HCN2
791 (black) HCN1 (black) in control solution (open circle), cAMP (filled circle) and cAMP +
792 TRIP8b_{nano}, or TRIP8b_{nano} only in the case of HCN1 (filled triangle). HCN4, control = -
793 102.8 \pm 0.3 mV; HCN4 + 1 μ M cAMP = -89.2 \pm 0.6 mV; HCN4 + 1 μ M cAMP + 10 μ M
794 TRIP8b_{nano} = -102.1 \pm 0.6 mV, HCN4 + 1 μ M cAMP in the patch pipette + 10 μ M
795 TRIP8b_{nano} in the bath solution = -91.7 \pm 0.3 mV; HCN2, control = -93.7 \pm 0.3 mV; HCN2 +
796 5 μ M cAMP = -83.5 \pm 0.3 mV; HCN2 + 5 μ M cAMP + 10 μ M TRIP8b_{nano} = -94.5 \pm 0.6 mV;
797 HCN1, control = -72.8 \pm 0.2 mV; HCN1 + 10 μ M TRIP8b_{nano} = -82 \pm 0.5 mV. Data are
798 presented as mean \pm SEM. Number of cells (N) \geq 11. There is no significant difference
799 between the controls and the addition of TRIP8b_{nano} with (HCN4, HCN2) or without
800 (HCN1) cAMP in the pipette. No significant difference was also observed for the addition
801 of TRIP8b_{nano} in the bath. Statistical analysis performed with two-way ANOVA, followed by
802 post-hoc Tukey test (P < 0.001).

803

804

805 **Figure 5.** Effects of TRIP8b_{nano} on voltage-dependent activation of I_f and spontaneous rate
806 in rabbit sinoatrial node (SAN) myocytes. **(A)** Representative whole-cell I_f currents

807 recorded, at the indicated voltages, in the control solution and in the presence of 10 μM
808 TRIP8b_{nano}, without (top) and with 1 μM cAMP in the pipette (bottom). **(B)** Mean I_f
809 activation curves were measured using a two-step protocol (see Material and Methods) in
810 control (filled circles) or in the presence of: 1 μM cAMP (open circles); 10 μM TRIP8b_{nano}
811 (filled squares); 1 μM cAMP + 10 μM TRIP8b_{nano} (open squares). Ligands were added in
812 the patch pipette. Half activation potential ($V_{1/2}$) of I_f activation curves measured in control
813 = -64.1 ± 0.4 mV or in the presence of: 1 μM cAMP = -59.9 ± 0.4 mV; 10 μM TRIP8b_{nano} =
814 -67.7 ± 0.4 mV; 1 μM cAMP + 10 μM TRIP8b_{nano} = -67.6 ± 0.7 mV. Data are presented as
815 mean \pm SEM. Number of cells (N) was ≥ 15 . $V_{1/2}$ values are significantly different between
816 each other's with the exception of $V_{1/2}$ obtained in the presence TRIP8b_{nano} and cAMP +
817 TRIP8b_{nano}. Statistical analysis performed with two-way ANOVA, followed by post-hoc
818 Bonferroni test (*, $P < 0.05$) **(C)** (Left) Representative recordings of single SAN cell
819 spontaneous activity in control and in the presence of 10 μM TRIP8b_{nano}. (Right) Mean
820 spontaneous rate (Hz) recorded in control solution = 3.65 ± 0.29 Hz and in the presence of
821 10 μM TRIP8b_{nano} added to the pipette = 2.69 ± 0.27 Hz. Data are presented as mean \pm
822 SEM. Number of cells (N) was ≥ 7 . Statistical analysis performed with t test (*, $P < 0.05$).

823

824 **Figure 6.** Effect of TRIP8b_{nano} and TAT-TRIP8b_{nano} on I_f and $I_{Ca,L}$ in mouse sinoatrial node
825 (SAN) myocytes. **(A)** Representative examples of I_f recordings at -95 mV in control
826 conditions (top), in 10 μM TRIP8b_{nano} dialysed cell (middle) and in cells perfused with 10
827 μM TAT-TRIP8b_{nano} (bottom), before (black trace) and after (red trace) application of ISO
828 100 nM. The voltage-clamp protocol used for recordings is shown above current traces.
829 **(B)** Mean normalised I_f current density recorded at -95 mV in absence and in presence of
830 10 μM TRIP8b_{nano} in the patch pipette, before (open bars) and after (filled bars) 100 nM
831 ISO perfusion. Data are presented as mean \pm SEM. Number of cells (N) ≥ 6 . Statistical
832 analysis performed with two-way ANOVA test, followed by Sidak multiple comparisons test
833 (**, $P < 0.01$). **(C)** Mean normalised I_f current density recorded at -95 mV in control solution
834 or in the solution containing 10 μM TAT-TRIP8b_{nano}, in absence (open bars) and in the
835 presence (filled bars) of 100 nM ISO. Data are presented as mean \pm SEM. Number of cells
836 (N) ≥ 8 . Statistical analysis performed with two-way ANOVA test, followed by Sidak
837 multiple comparisons test (****, $P < 0.0001$). **(D)** Representative examples of $I_{Ca,L}$
838 recordings at -10 mV in control conditions (top), in 10 μM TRIP8b_{nano} dialysed cell (middle)
839 and in cells perfused with 10 μM TAT-TRIP8b_{nano} (bottom), before (black trace) and after

840 (red trace) application of ISO 100 nM. The voltage-clamp protocol used for recordings is
841 shown above current traces. (E) Mean normalised $I_{Ca,L}$ current density recorded at -10 mV
842 in absence and in presence of 10 μ M TRIP8b_{nano} in the patch pipette, before (open bars)
843 and after (filled bars) 100 nM ISO perfusion. Data are presented as mean \pm SEM. Number
844 of cells (N) \geq 8. Statistical analysis performed with two-way ANOVA test, followed by Sidak
845 multiple comparisons test (***, P < 0.001; ****, P < 0.0001). (F) Mean normalised $I_{Ca,L}$
846 current density recorded at -10 mV in control solution or in the solution containing 10 μ M
847 TAT-TRIP8b_{nano}, in absence (open bars) and in the presence (filled bars) of 100 nM ISO.
848 Data are presented as mean \pm SEM. Number of cells (N) \geq 7. Statistical analysis
849 performed with two-way ANOVA test, followed by Sidak multiple comparison test (**, P <
850 0.01; *** P < 0.001).

851

852 **Figure 3 - figure supplement 1.** CNBD residues involved in TRIP8b_{nano} binding.
853 Combined chemical shift variations of NMR signals between CNBD unbound and
854 TRIP8b_{nano}-bound state. Combined chemical shift variations are calculated from the
855 experimental 1 H and 15 N chemical shift changes ($\Delta\delta(^1H)$ and $\Delta\delta(^{15}N)$, respectively)
856 between the corresponding peaks in the two forms, through the following equation (Garrett

857 et al., 1997):
$$\Delta\delta^{combined} = \sqrt{\frac{(\Delta\delta(^1H))^2 + \frac{1}{25}(\Delta\delta(^{15}N))^2}{2}}$$

858

859

860 Residues experiencing intermediate exchange regime (whose NMR signal becomes broad
861 beyond detection upon addition of TRIP8b_{nano}) are shown in grey. The horizontal dotted
862 line indicates the average value plus one standard deviation. Residues above the line
863 were set as “active” in the docking calculation described in the text (see Materials and
864 Methods).

865 Garrett DS, Seok YJ, Peterkofsky A, Clore GM & Gronenborn AM (1997) Identification by NMR of the binding
866 surface for the histidine-containing phosphocarrier protein HPr on the N-terminal domain of enzyme I
867 of the Escherichia coli phosphotransferase system. *Biochemistry* **36**: 4393–4398

868

869

870 **Figure 3 - figure supplement 2.** Representative families of clusters obtained from the first
871 docking calculation. The clusters obtained can be grouped in two classes, shown here, on
872 the basis of the position of helix N of TRIP8b_{nano} (N) relative to the CNBD. In the left
873 representative structure, helix N is oriented in a way that allows E₂₄₁ to interact with R₆₅₀ of
874 C-helix. In the right representative structure, E₂₄₀ - E₂₄₁ interact with N₅₄₇ of CNBD. In all
875 clusters K₆₆₅ or K₆₆₆ of CNBD establish a contact with either E₂₆₄ or E₂₆₅ of TRIP8b_{nano}.
876 The structural elements of CNBD are labelled: αE', αA and αC. Helices N and C of
877 TRIP8b_{nano} are labelled.

878

879 **Figure 3 - figure supplement 3.** Biochemical validation of CNBD – TRIP8b_{nano} complex.
880 Dissociation constant (K_D) of the interaction between the indicated CNBD and TRIP8b_{nano}
881 peptides were measured by means of Isothermal Titration Calorimetry (ITC). CNBD WT -
882 TRIP8b_{nano} WT (black filled circle) = 1.4 ± 0.1 μM; CNBD K₆₆₅E - TRIP8b_{nano} WT (grey filled
883 circle) = 6 ± 0.3 μM; CNBD K₆₆₆E - TRIP8b_{nano} WT (grey filled circle) = 9.9 ± 0.8 μM; CNBD
884 WT - TRIP8b_{nano} E₆₄K (purple filled circle) = 4.8 ± 0.2 μM; CNBD WT - TRIP8b_{nano} E₆₅K
885 (purple filled circle) = 6 ± 0.5 μM; CNBD R₆₅₀E - TRIP8b_{nano} WT (red filled circle) = 9.6 ±
886 0.7 μM; CNBD WT - TRIP8b_{nano} E₄₀R (green filled circle) = 5 ± 0.3 μM; CNBD WT -
887 TRIP8b_{nano} E₄₁R (green filled circle) = 3.8 ± 0.2 μM; CNBD N₅₄₇D - TRIP8b_{nano} WT (blue
888 filled circle) = 11 ± 0.9 μM; CNBD WT - TRIP8b_{nano} D₅₂N (orange filled circle) = 3.4 ± 0.1
889 μM. Data are presented as mean ± SEM. Number of experiments (N) ≥ 3. K_D values of all
890 tested combinations are statistically different from the K_D of CNBD WT for TRIP8b_{nano} WT
891 (*, P ≤ 0.05; **, P < 0.01). Statistical analysis performed with ANOVA, followed by post-hoc
892 Tukey test. Dashed black vertical line indicates the K_D of WT peptides.

893

894

895 **Figure 3 - figure supplement 4.** Different orientation of R₆₆₂ and K₆₆₅ in the cAMP-bound
896 and TRIP8b_{nano}-bound conformation of the CNBD. Residues R₆₆₂ and K₆₆₅ of CNBD C-
897 helix (αC) which interact with cAMP (left, (Lolicato et al., 2011) and TRIP8b_{nano} (right, this
898 study) are represented as blue sticks and labelled. TRIP8b_{nano} residues E₂₅₀ and D₂₅₇
899 interacting with R₆₆₂ and residue E₂₆₅ interacting with K₆₆₅ are shown in red sticks and
900 labelled.

901 Lolicato M, Nardini M, Gazzarrini S, Moller S, Bertinetti D, Herberg FW, Bolognesi M, Martin H, Fasolini M,

902 Bertrand JA, Arrigoni C, Thiel G & Moroni A (2011) Tetramerization dynamics of C-terminal domain
903 underlies isoform-specific cAMP gating in hyperpolarization-activated cyclic nucleotide-gated
904 channels. *J. Biol. Chem.* **286**: 44811–44820. Retrieved from doi: 10.1074/jbc.M111.297606.
905
906
907

908 **Figure 3 - figure supplement 5.** Mutation N₅₂₀D affects cAMP affinity in full-length HCN2
909 channel. Note that in mouse HCN2 N₅₂₀D corresponds to N₅₄₇D in human HCN2 (used in
910 our structural studies). **(A)** Representative whole-cell HCN2 currents recorded, at the
911 indicated voltages (-70, -80, -90, -130 mV) in HEK 293T cells transfected with WT and
912 N₅₂₀D mutant, in the absence and presence of 5 μM cAMP in the pipette. **(B)** Mean
913 activation curves obtained from the tail currents in (A) and other recordings in control
914 solution (filled circle) and in the presence of cAMP (open circles), with HCN2 wt (black)
915 and N₅₄₇D mutant. Data were fitted to a Boltzmann equation (solid and dotted lines) (see
916 Methods) . **(C)** Half activation potential ($V_{1/2}$) values derived from Boltzmann equation
917 fitting. HCN2 WT (black filled circle) $V_{1/2} = -95.9 \pm 0.3$ mV; HCN2 WT + 5 μM cAMP (black
918 open circle) $V_{1/2} = 85.2 \pm 0.4$ mV; HCN2 N₅₂₀D (red filled circle) $V_{1/2} = -96.8 \pm 0.2$ mV;
919 HCN2 N₅₂₀D + 5 μM cAMP (red open circle) $V_{1/2} = -91.2 \pm 0.2$ mV. Data are presented as
920 mean ± SEM. Number of experiments (N) ≥ 6. Statistical analysis performed with two-way
921 ANOVA, followed by post-hoc Tukey test (P < 0.001) showed that wt and mutant channel
922 are identical and that the cAMP-induced shifts are different.

923
924

925 **Figure 3 - figure supplement 6.** Structural characterization of N₅₄₇D CNBD protein.
926 Superimposition of the [¹H, ¹⁵N] HSQC spectra of CNBD wt (black) and CNBD N₅₄₇D
927 mutant (red).

928

929 **Figure 3- source data 1.** Acquisition parameters for NMR experiments performed on
930 cAMP- free human HCN2 CNBD in complex with TRIP8b_{nano} and vice-versa.

931

932 **Figure 3- source data 2.** Docking calculation.

933
934

935 **Figure 4 - figure supplement 1.** Comparison of half activation potentials ($V_{1/2}$) of HCN1
936 WT and of R₅₄₉E mutant (Chen, Wang, & Siegelbaum, 2001). (A) Currents were measured
937 at the indicated voltages (-50, -60, -70, -120 mV), from HEK 293T cells with control
938 solution or with 15 μ M cAMP in the patch pipette. (B) Mean activation curves obtained
939 from tail currents were fitted to a Boltzmann equation (see Material and Methods). (C) Half
940 activation potential ($V_{1/2}$) determined from Boltzmann fitting. HCN1 WT (black filled circle)
941 = -72.7 ± 0.2 mV; HCN1 WT + cAMP (black open circle) = -73.1 ± 0.3 mV; HCN1 R₅₄₉E
942 (red filled circle) = -80.4 ± 0.2 mV; HCN1 R₅₄₉E + cAMP (red open circle) = -81 ± 0.3 mV.
943 Data are presented as mean \pm SEM. Number of experiments (N) \geq 8. Wt values are
944 significantly different from mutant. Statistical analysis performed with two-way ANOVA,
945 followed by post-hoc Tukey test (P < 0.001).

946

947 Chen S, Wang J & Siegelbaum SA (2001) Properties of Hyperpolarization-Activated Pacemaker Current
948 Defined by Coassembly of Hcn1 and Hcn2 Subunits and Basal Modulation by Cyclic Nucleotide. *J. Gen.*
949 *Physiol.* **117**: 491–504. Retrieved from <http://www.jgp.org/lookup/doi/10.1085/jgp.117.5.491>

950

951

952 **Figure 4 - figuresupplement 2.** Voltage-dependency of activation time constant (τ_{on}) of
953 HCN4 channels in control solution (open circles), 1 μ M cAMP (filled circles), 1 μ M cAMP +
954 10 μ M TRIP8b_{nano} (filled triangles). Data are presented as mean \pm SEM. Number of cells
955 (N) = 5.

956 **Figure 6 - figure supplement 1.** Effect of TAT- (SCRAMBLED) TRIP8b_{nano} on I_f in mouse
957 sinoatrial node (SAN) myocytes. (A) Representative examples of I_f recordings (at -95mV)
958 in TAT-(SCRAMBLED)TRIP8b_{nano} (top) or in TAT-TRIP8b_{nano} (bottom) incubated cells. The
959 voltage-clamp protocol used for recordings is shown above current traces. (B) Mean
960 normalised I_f current density recorded at -95 mV in the presence of 10 μ M TAT-
961 (SCRAMBLED) TRIP8b_{nano} or TAT-TRIP8b_{nano}, before (open bars) and after (filled bars)
962 100 nM isoprenaline (ISO) perfusion. Data are presented as mean \pm SEM. Number of cells
963 (N) \geq 11. Statistical analysis performed with two-way ANOVA test, followed by Sidak
964 multiple comparisons test (****, P < 0.0001).

965

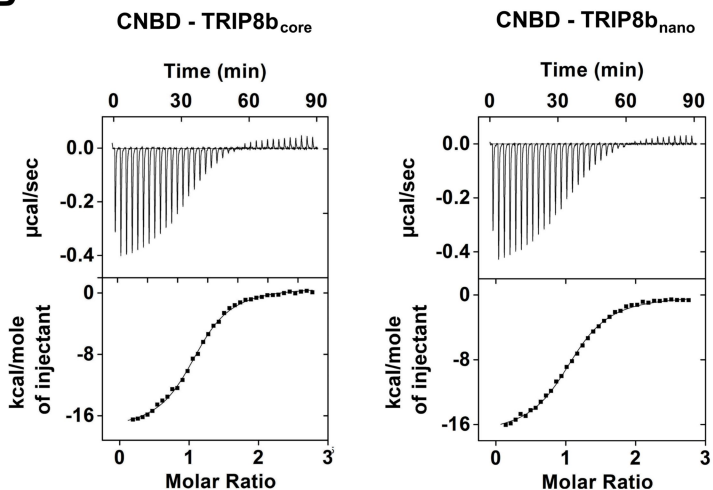
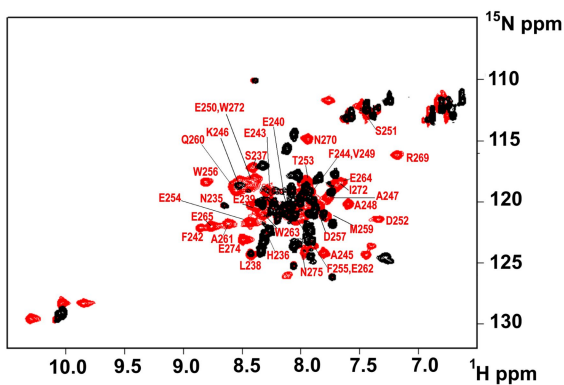
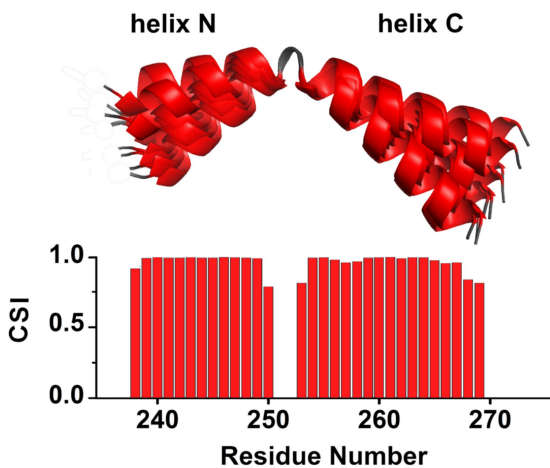
966

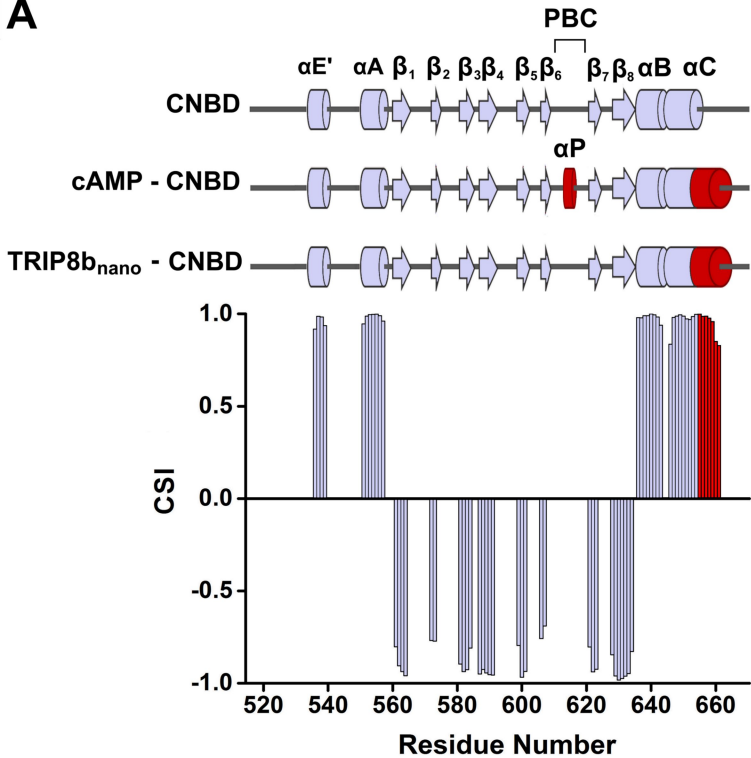
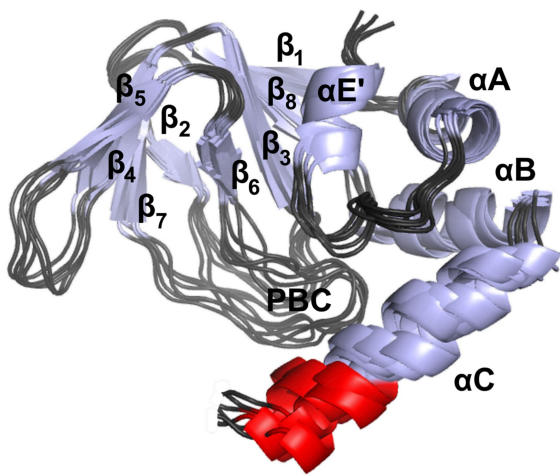
967

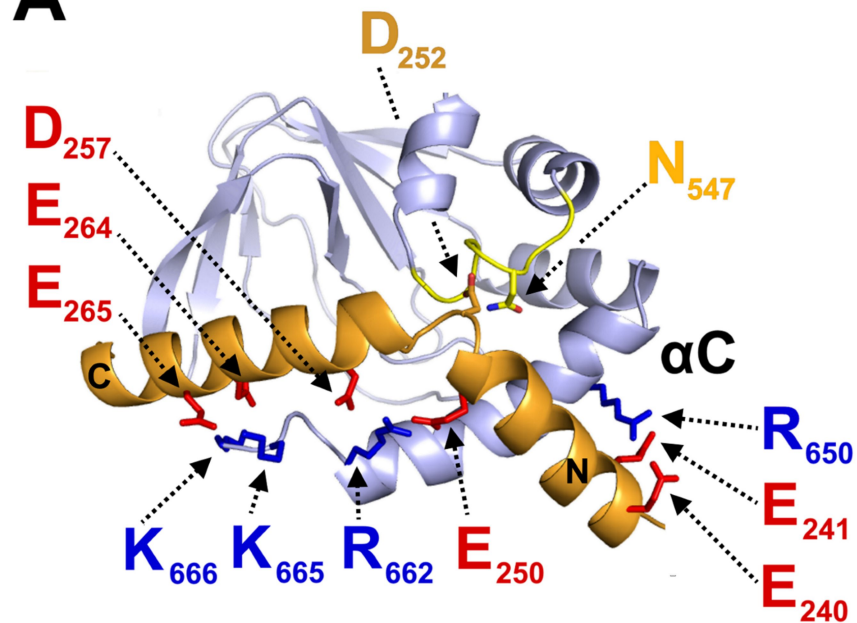
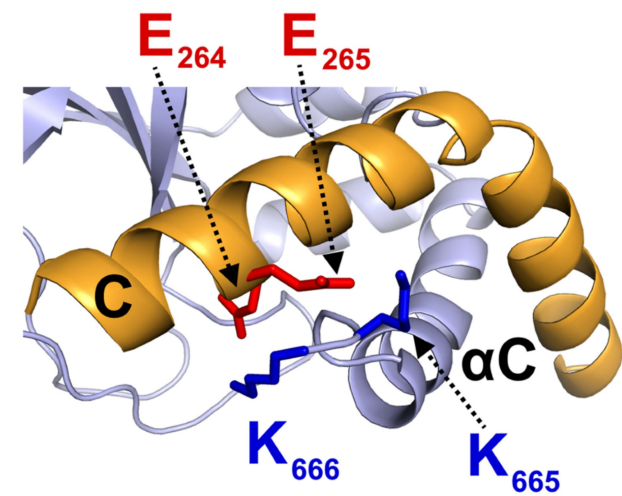
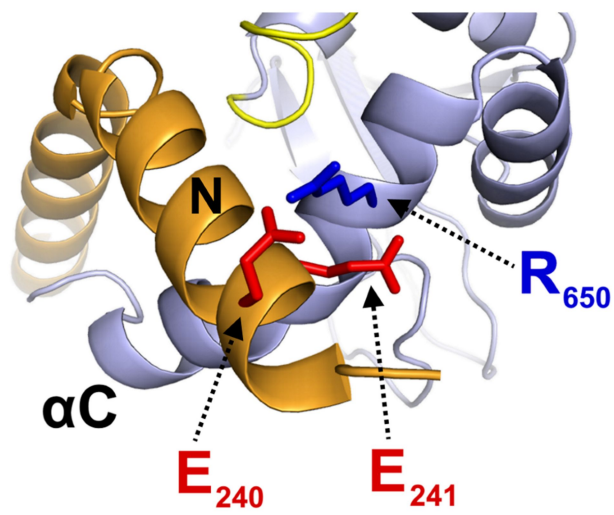
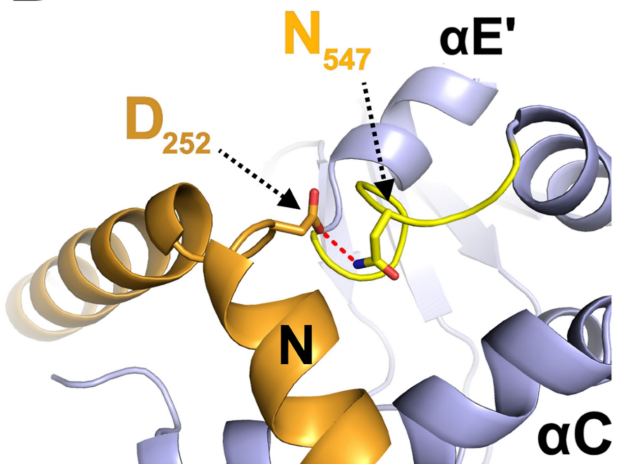
968

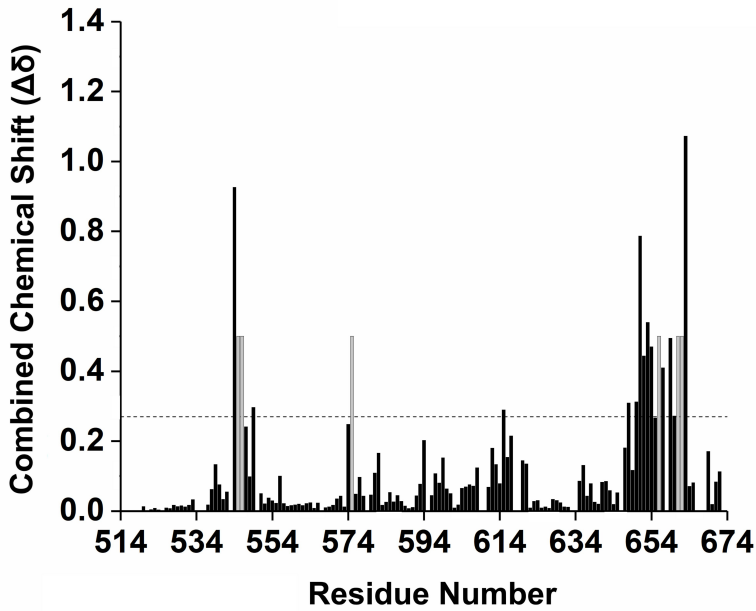
A

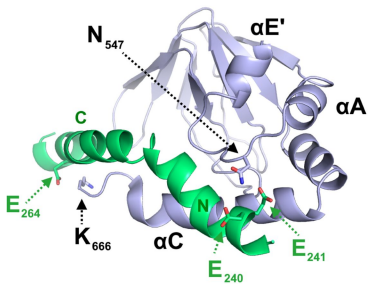
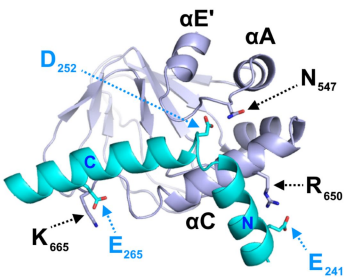
235 245 255 265 275
 NHSLEEEFERAKAAVESDTEFWDKMQAEWEEMARRNWIEN

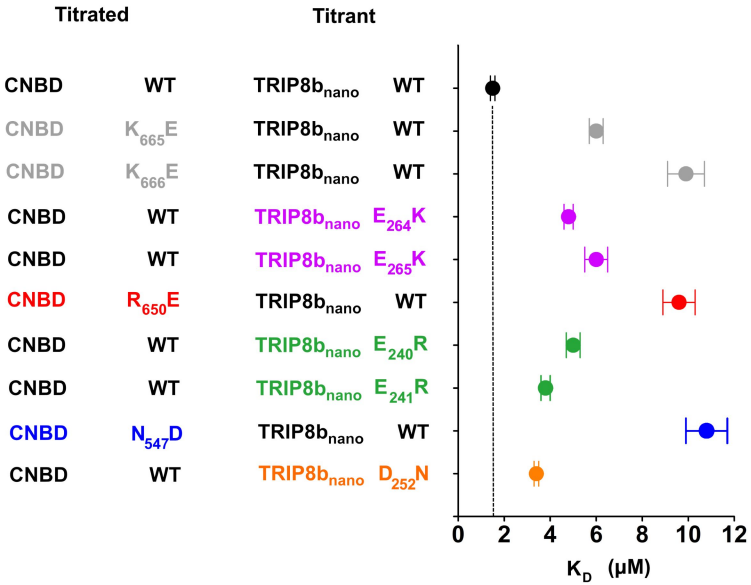
B**C****D**

A**B**

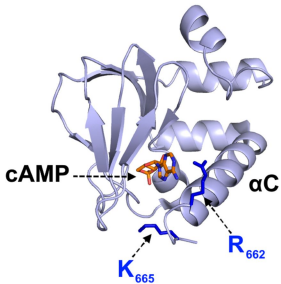
A**B****C****D**



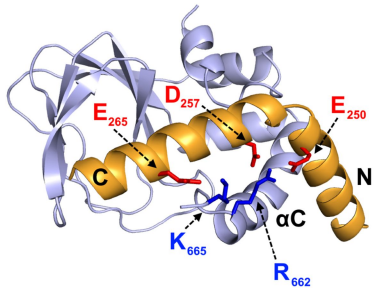


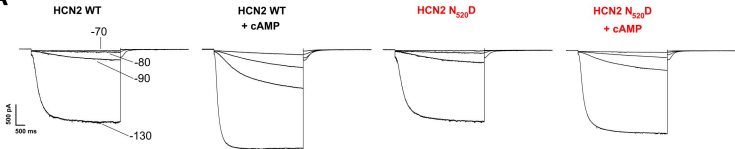
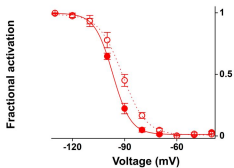
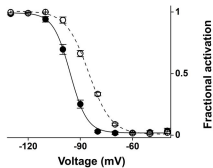
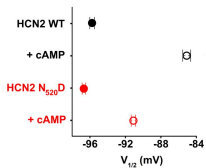


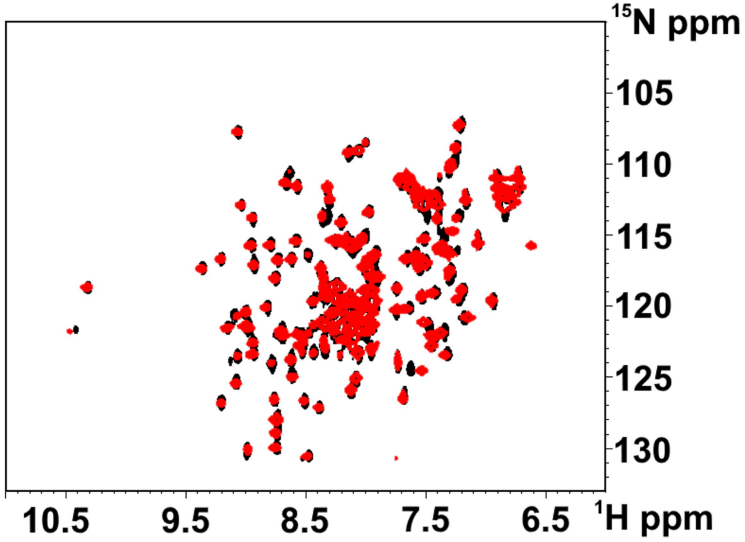
cAMP-bound CNBD

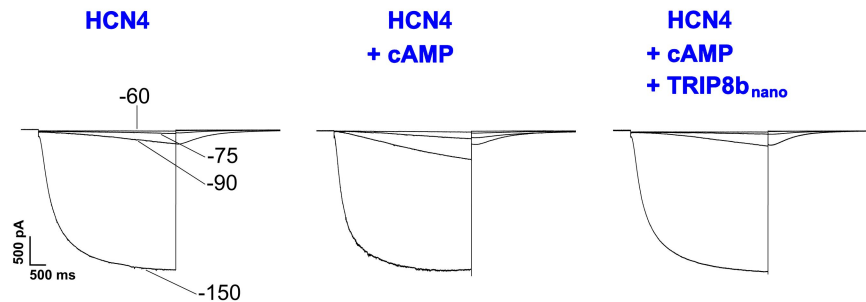
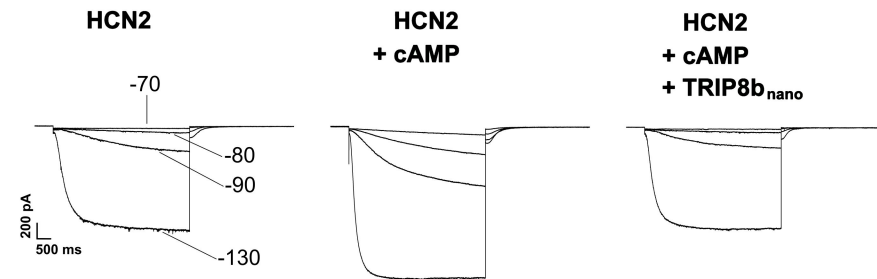
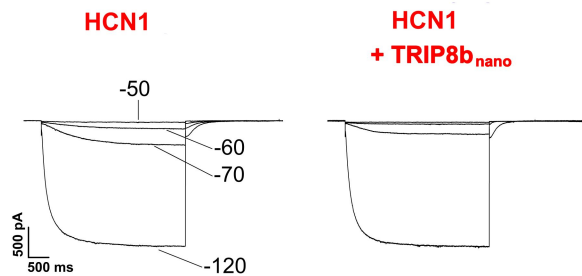
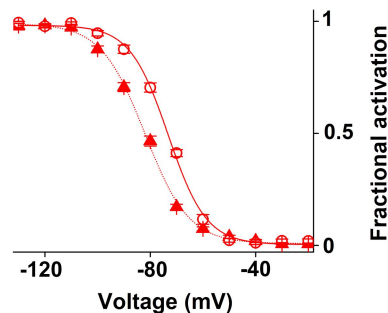
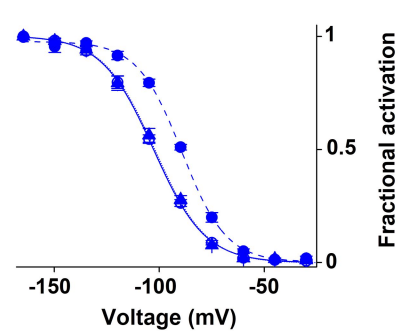
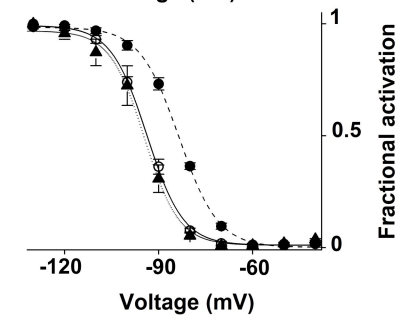
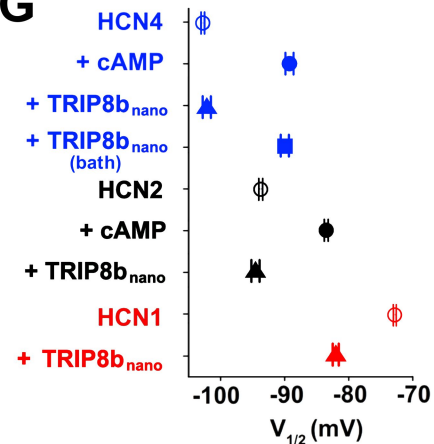


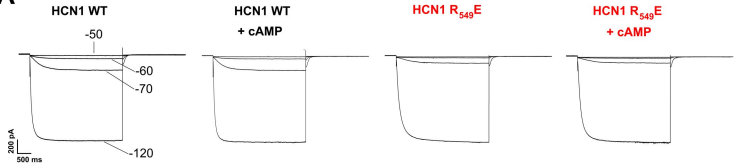
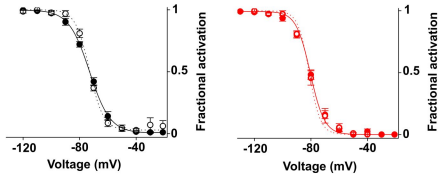
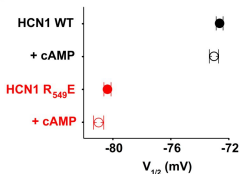
TRIP8b_{nano}-bound CNBD

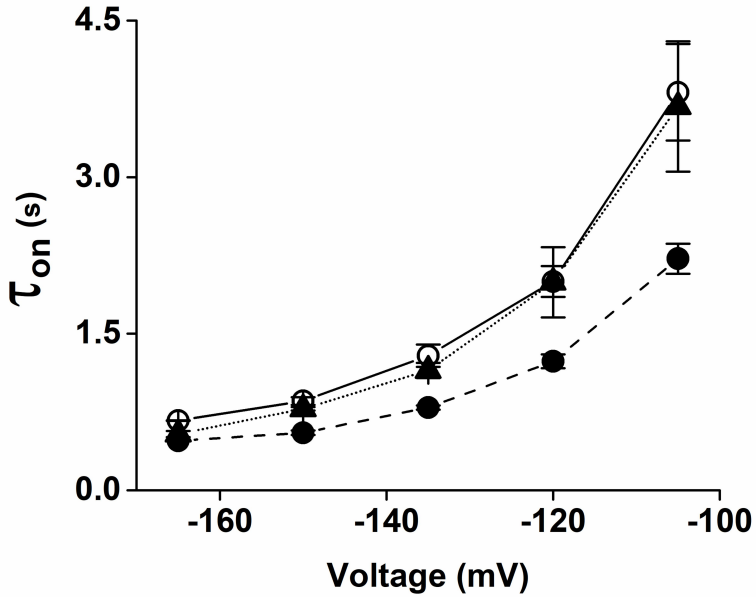


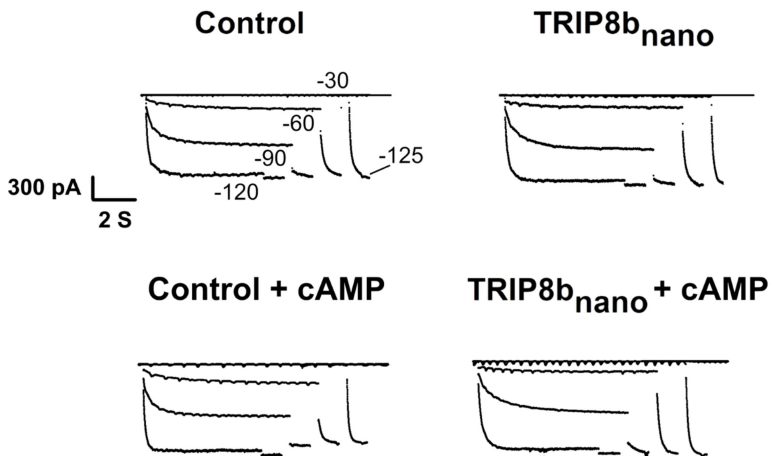
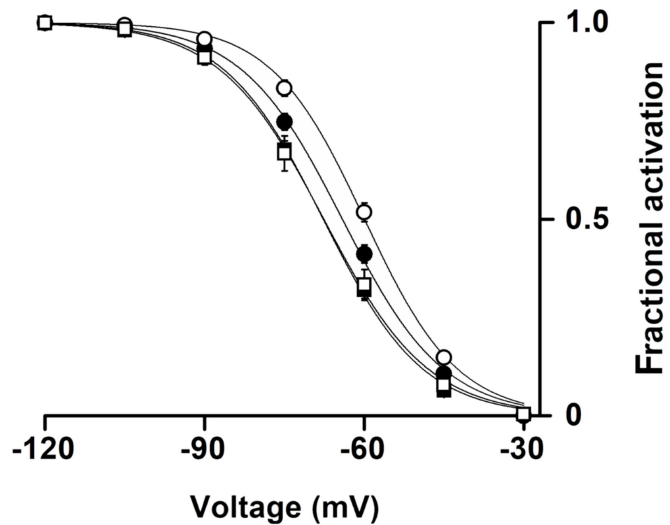
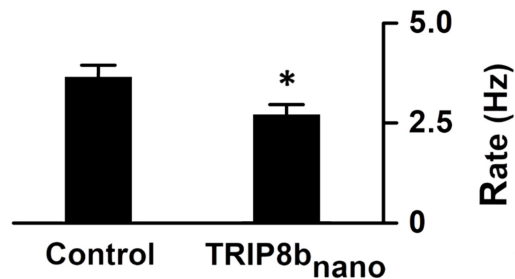
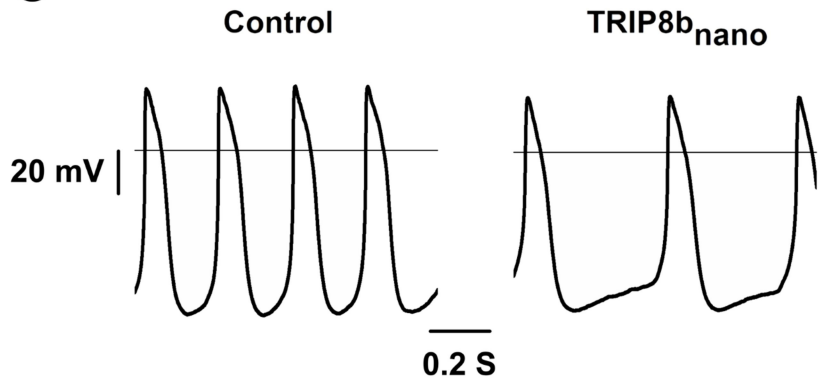
A**B****C**

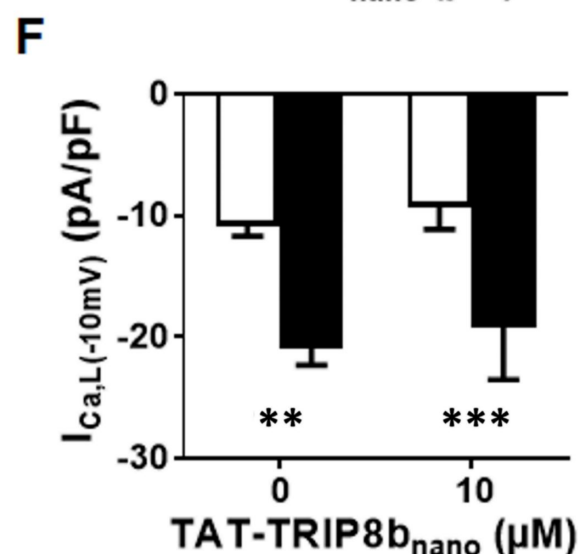
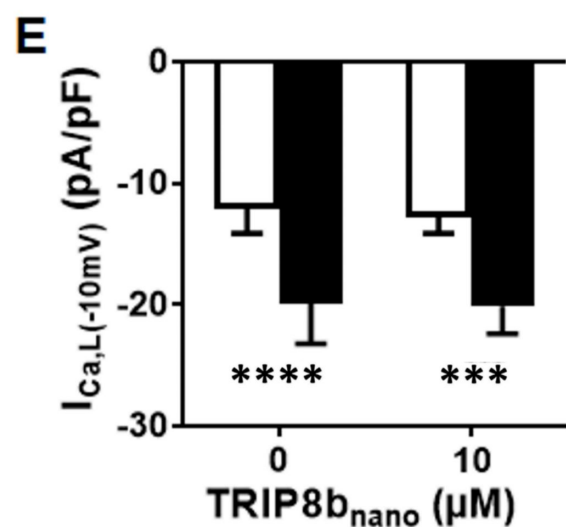
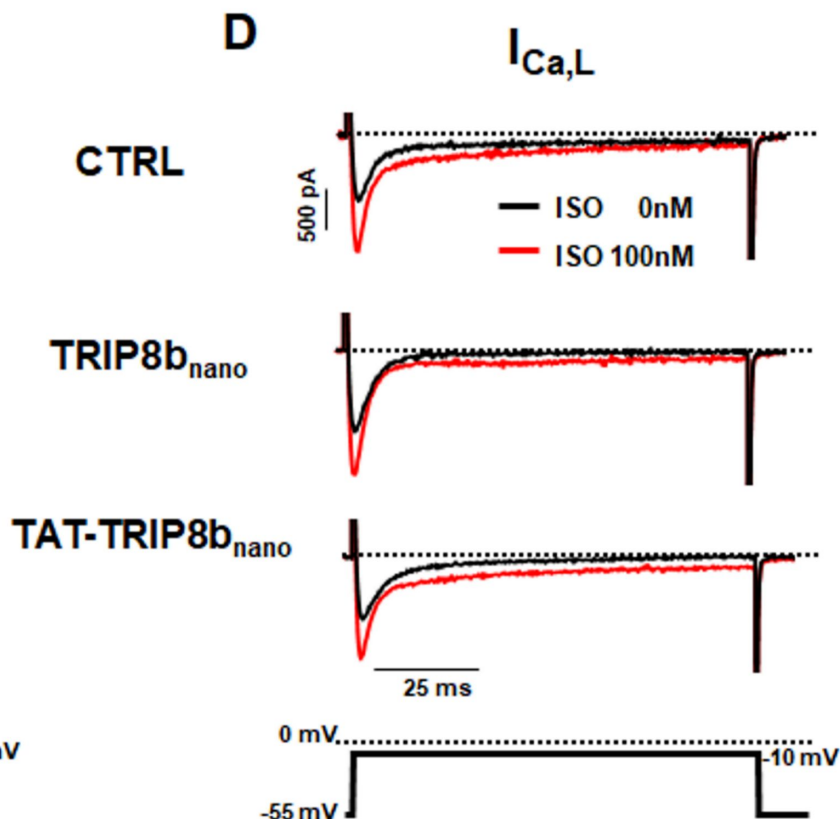
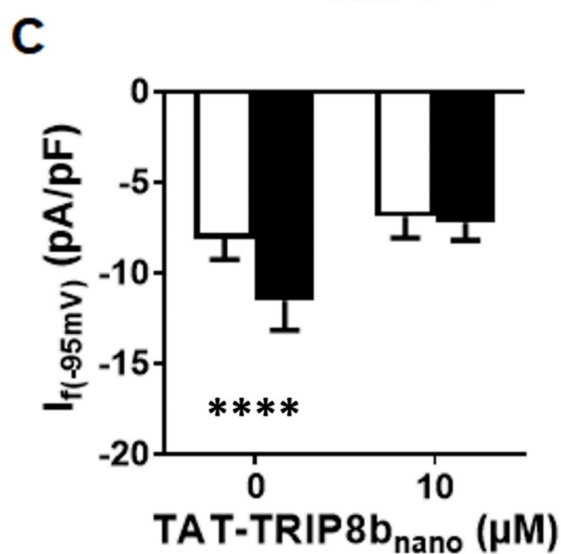
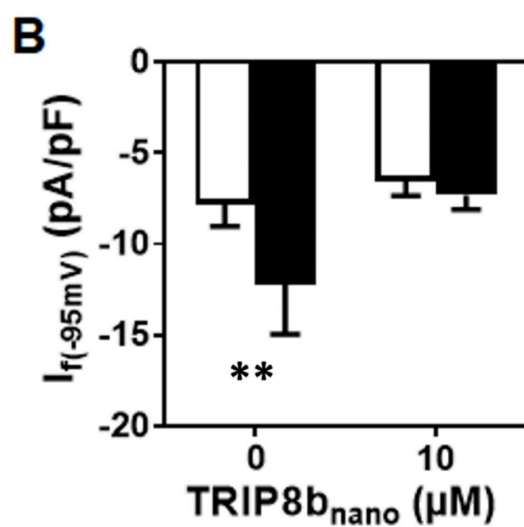
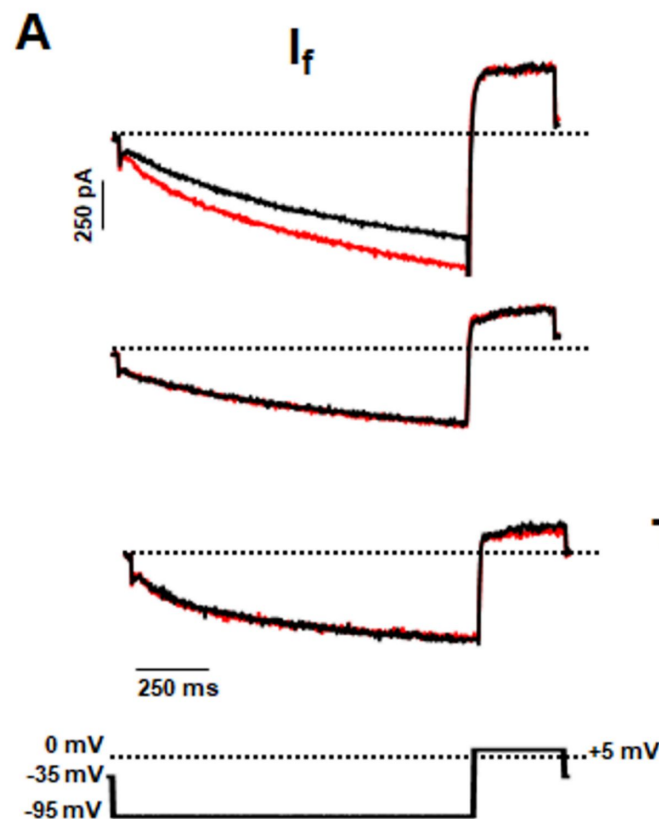


A**B****C****F****D****E****G**

A**B****C**

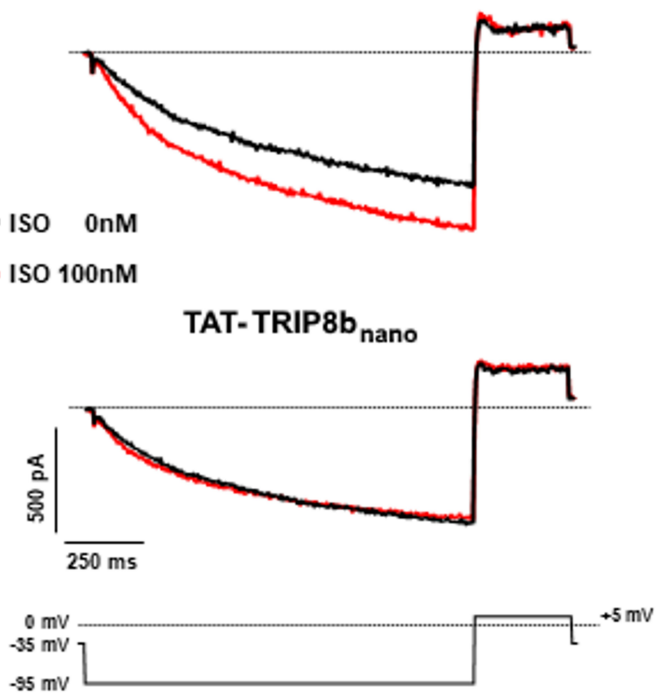


A**B****C**



ATAT- (SCR) TRIP8b_{nano}

— ISO 0nM
— ISO 100nM

**B**